The Astrophysical Journal, 946:59 (16pp), 2023 April 1 https://doi.org/10.3847/1538-4357/aca591

4-OGC: Catalog of Gravitational Waves from Compact Binary Mergers

Alexander H. Nitz[1,2], Sumit Kumar[1,2], Yi-Fan Wang (王一帆)[1,2], Shilpa Kastha[1,2], Shichao Wu (吴仕超)[1,2], Marlin Schäfer[1,2], Rahul Dhurkunde[1,2], and Collin D. Capano[1,2,3]
[1] Max-Planck-Institut für Gravitationsphysik (Albert-Einstein-Institut), D-30167 Hannover, Germany; alex.nitz@aei.mpg.de
[2] Leibniz Universität Hannover, D-30167 Hannover, Germany
[3] Department of Mathematics, University of Massachusetts, Dartmouth, MA 02747, USA
Received 2022 September 13; revised 2022 October 26; accepted 2022 November 22; published 2023 March 30

Abstract

We present the fourth Open Gravitational-wave Catalog (4-OGC) of binary neutron star (BNS), binary black hole (BBH), and neutron star–black hole (NSBH) mergers. The catalog includes observations from 2015 to 2020 covering the first through third observing runs (O1, O2, O3a, and O3b) of Advanced LIGO and Advanced Virgo. The updated catalog includes seven BBH mergers that were not previously reported with high significance during O3b for a total of 94 observations: 90 BBHs, 2 NSBHs, and 2 BNSs. The most confident new detection, GW200318_191337, has component masses $49.1^{+16.4}_{-12.0} M_\odot$ and $31.6^{+12.0}_{-11.6} M_\odot$; its redshift of $0.84^{+0.4}_{-0.35}$ (90% credible interval) may make it the most distant merger so far. We estimate the merger rate of BBH sources, assuming a power-law mass distribution containing an additive Gaussian peak, to be $16.5^{+10.4}_{-6.2}(25.0^{+12.6}_{-8.0})$ Gpc^{-3} yr^{-1} at a redshift of $z = 0$ (0.2). For BNS and NSBH sources, we estimate a merger rate of 200^{+309}_{-148} Gpc^{-3} yr^{-1} and 19^{+30}_{-14} Gpc^{-3} yr^{-1}, respectively, assuming the known sources are representative of the total population. We provide reference parameter estimates for each of these sources using an up-to-date model accounting for instrumental calibration uncertainty. The corresponding data release also includes our full set of subthreshold candidates.

Unified Astronomy Thesaurus concepts: Gravitational waves (678); Gravitational wave astronomy (675); Astrophysical black holes (98); Stellar mass black holes (1611); Neutron stars (1108); Compact objects (288)

1. Introduction

Gravitational-wave astronomy has entered an era of regular and routine observation of compact binary mergers. This achievement was made possible by the second-generation gravitational-wave observatories, led by the twin Advanced LIGO (Hanford and Livingston; Aasi et al. 2015) and Advanced Virgo (Acernese et al. 2015) observatories, which have been operating since 2015 and 2017, respectively. This period has seen continued improvement in their astrophysical reach over their three completed observing runs (O1–O3; Abbott et al. 2020b), with the pace rapidly increasing from three merger observations in O1 to dozens in the first half of O3 (O3a; Abbott et al. 2019a, 2021a, 2021c; Venumadhav et al. 2020a; Nitz et al. 2019c, 2021a); the vast majority of these are binary black hole (BBH) mergers. To date, there is only a single binary neutron star (BNS) observation, GW170817 (Abbott et al. 2017a), which has been corroborated by extensive electromagnetic observations (Abbott et al. 2017b). In addition, GW190425 is a potential heavy BNS merger (Abbott et al. 2020a), and recently two sources with masses compatible with merging neutron star–black hole (NSBH) binaries have been reported (Abbott et al. 2021d). The plethora of BBH observations, in addition to exceptional events such as GW190521 with total mass $\sim 150 M_\odot$ (Abbott et al. 2020c; Capano et al. 2021), are beginning to constrain formation scenarios (Abbott et al. 2020d; Edelman et al. 2021; Gerosa & Fishbach 2021; Zevin et al. 2021) and deviations from general relativity (Abbott et al. 2021e; Wang et al. 2022).

We expect the current observatories to continue to improve in sensitivity over the next few years (Abbott et al. 2020b) due to ongoing active commissioning and the inclusion of new technologies into the existing sites (Aasi et al. 2013). The upcoming O4 observing run is scheduled to begin at the end of 2022 with a fiducial BNS range of 160–190 Mpc (Abbott et al. 2020b). In addition, we can expect that a fourth ground-based gravitational-wave observatory, KAGRA, will join the O4 observing run (Akutsu et al. 2021). In the mid- to late 2020s, a fifth observatory will join the worldwide network with the construction of LIGO India (Unnikrishnan 2013; Saleem et al. 2022). Efforts are also advancing for third-generation observatories, the Cosmic Explorer and the Einstein Telescope, which promise an order of magnitude sensitivity improvement (Punturo et al. 2010; Reitze et al. 2019; Evans et al. 2021).

This work provides a comprehensive catalog of gravitational-wave observations from merging BNS, BBH, and NSBH sources. The analysis is based on a deep archival search using the public data from the LIGO and Virgo observatories (Vallisneri et al. 2015; Abbott et al. 2021f), which spans 2015–2020 and includes all existing observing runs (O1–O3). This catalog updates the results of our previous 3-OGC (third Open Gravitational-wave Catalog; Nitz et al. 2021a) by including analysis of data from the second half of the third observing run (O3b) that very recently became public. The next expected public data release would be at the end of 2024 if the current release delay of 18 months with a 6 month cadence is maintained. Included in our companion data release is the complete set of subthreshold candidates and parameter estimates for significant candidates (Nitz & Kumar 2021). We make available our subthreshold candidates so that they may aid follow-up studies, including those which cross-correlate candidates with other archival data sets such as from gamma-ray bursts (Nitz et al. 2019b; Burns et al. 2019), high-

energy neutrinos (Countryman et al. 2019), or optical transients (Andreoni et al. 2019; Setzer et al. 2019). Archival analyses have the potential to uncover distant or faint populations.

We find a total of 94 mergers that pass our significance threshold $\mathcal{P}_{\rm astro} > 0.5$ or false alarm rate (FAR) less than once per 100 yr. The vast majority, 90, of these are BBH mergers; seven are reported during O3b for the first time here with high significance, and three additional were previously reported marginal candidates in the 3-OGC (Nitz et al. 2021a). We find the previously reported BNS and NSBH mergers (Abbott et al. 2017a, 2020a, 2021d); however, no new confident BNS or NSBH mergers are observed. We expect a total catalog contamination fraction of $\sim$10 (1)% at a $\mathcal{P}_{\rm astro} > 0.5$ (0.9) threshold. Our results are broadly consistent with the recent GWTC-3 catalog produced by the LIGO–Virgo–KAGRA (LVK) collaborations (Abbott et al. 2021g, 2021h).

2. Search for Compact Binary Mergers

Our catalog includes results from the analysis of the complete set of public LIGO and Virgo data collected over a period of 5 yr (Vallisneri et al. 2015; Abbott et al. 2021f). To identify the signature of gravitational waves from compact binary mergers, we use matched filtering to extract the signal-to-noise ratio (S/N) of a potential signal (Allen et al. 2012). Candidates are identified by looking for peaks in the single-detector S/N time series and correlating these triggers between observing detectors. Each candidate is assessed for consistency between the expected signal morphology and the data (Allen 2005; Nitz 2018) and ranked using additional factors such as the observed rate of triggers, multidetector coherence (Nitz et al. 2017; Davies et al. 2020), and local data quality (Abbott et al. 2018; Mozzon et al. 2020). This procedure is the same as that used for the prior 3-OGC (Nitz et al. 2021a) and is implemented using the open-source PyCBC toolkit (Usman et al. 2016; Nitz et al. 2021d). This toolkit has also been used to construct many matched-filter- based gravitational-wave searches (Abbott et al. 2019a, 2021a, 2021g, 2022), including those that account for eccentricity (Nitz et al. 2019a), and are focused on intermediate-mass BBHs (Chandra et al. 2021) or target subsolar-mass mergers (Nitz & Wang 2021a, 2021b, 2021c).

2.1. LIGO and Virgo Observing Periods

The public LIGO and Virgo data span the time period 2015–2020 and the three completed observing runs O1–O3 (Vallisneri et al. 2015; Abbott et al. 2021f). As in 3-OGC (Nitz et al. 2021a), we include results from data released outside the nominal observation runs; notably, this includes data around GW170608 (Abbott et al. 2017c) and GW190814 (Abbott et al. 2020e). Table 1 shows the number of days that different network configurations were observing. Our updated catalog includes the recently released second half of the third observing run (O3b). The full O3 observing run contains 152 days of triple-detector observing time and $\sim$200 days when both LIGO observatories were observing. We analyze all data when multiple detectors are observing and also identify sources in the data when only LIGO-Livingston or LIGO-Hanford is observing. Due to the decreased range and relatively large population of non-Gaussian transient noise, we do not consider data when only Virgo is observing. In Figure 1 we show the sky-averaged fiducial BNS range of each instrument as a function of time. All instruments have made significant gains in sensitivity during O3 as compared to O2, with Virgo reaching 60 Mpc range and LIGO-Livingston periodically exceeding 140 Mpc.

Table 1
Analyzed Time in Days for Different Global Network Observing Scenarios

Observation	HLV	HL	HV	LV	H	L	V
O1	⋯	48.6	⋯	⋯	27.6	17.0	⋯
O2	15.2	103.3	1.7	2.2	37.8	33.0	1.7
O3	152.0	49.5	31.7	38.9	10.3	9.9	25.0
All	167.2	201.4	33.4	41.1	75.6	59.9	26.7

Note. The abbreviations H, L, and V are used for the LIGO-Hanford, LIGO-Livingston, and Virgo observatories, respectively. Each time period is exclusive of the others. Some data are excluded from the full public data set due to analysis requirements (O(1)%). However, data around GW170608 and GW190814 that were made available separately from the bulk data release are included (Vallisneri et al. 2015).

The data have been calibrated by the LVK collaborations and made available through the Gravitational-wave Open Science Center (GWOSC; Vallisneri et al. 2015; Acernese et al. 2018; Viets et al. 2018; Abbott et al. 2021f; Bhattacharjee et al. 2021; Estevez et al. 2021). Noise subtraction using auxiliary witness channels is applied to the bulk data release (Davis et al. 2019; Estevez et al. 2019; Rolland et al. 2019; Vajente et al. 2020). Our analysis also makes use of the data quality information compiled by the LVK detector characterization teams (Davis et al. 2021) to exclude times around hardware signal injections and times affected by adverse instrumental behavior.

2.2. Search Space

Our search uses matched filtering to identify signals within the data; matched filtering requires a model of the expected signal to filter the data. To identify sources within a broad target region of parameters (component masses $m_{1,2}$ and spins), we use a discrete bank of template waveforms. For this catalog, we use the same template bank, shown in Figure 2, that we previously used in the 3-OGC analysis (Nitz et al. 2021a).

The templates are chosen to ensure that a minimum fraction of the optimal S/N of a potential signal is recovered, typically $\mathcal{O}$(97%) for many searches (Dal Canton & Harry 2017). The bank is constructed in four parts using a brute-force stochastic algorithm (Harry et al. 2009; Ajith et al. 2014). These regions include a focused low-mass-ratio, low-spin, BBH region with a target S/N recovery >99.5%. In addition, there are BNS, NSBH, and broad-parameter BBH banks that target S/N recovery >97%.

The template bank is designed to recover gravitational-wave signals from nonprecessing quasi-circular sources. Our search accounts only for the effects of the dominant-mode gravitational-wave signal and does not include the effects of higher-order modes. Neglecting these effects will reduce the search sensitivity to sources that strongly exhibit these features, such as for highly inclined, high-mass-ratio, or highly precessing binaries (Harry et al. 2016) or where there remains residual eccentricity (Ramos-Buades et al. 2020; Wang & Nitz 2021). Development of optimal search strategies for these sources is an ongoing endeavor (Harry et al. 2016, 2018), and techniques that do not rely on matched filtering also target these sources (Klimenko et al. 2008, 2016; Tiwari et al. 2016). To model the

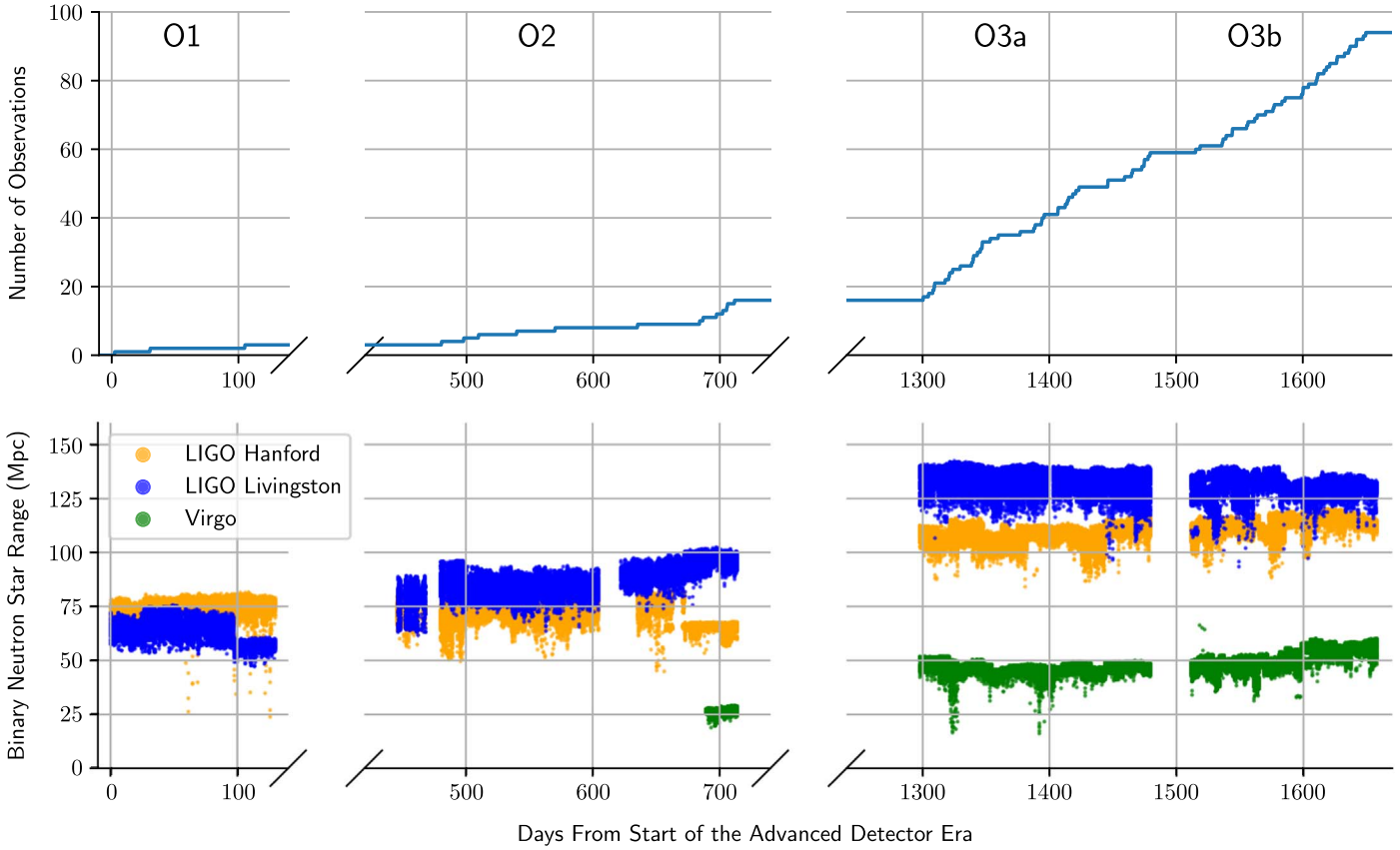

Figure 1. The cumulative number of binary merger observations (top) and the fiducial 1.4–1.4 $M_\odot$ BNS merger range (bottom) of the LIGO-Hanford (orange), LIGO-Livingston (blue), and Virgo (green) observatories at an S/N of 8 as a function of days since the start of the advanced detector era. The distance is averaged over sky location and orientation angles. The O1 (left), O2 (middle), and O3 (right) observing periods are shown. The break in O3 demarks the boundary between O3a and O3b.

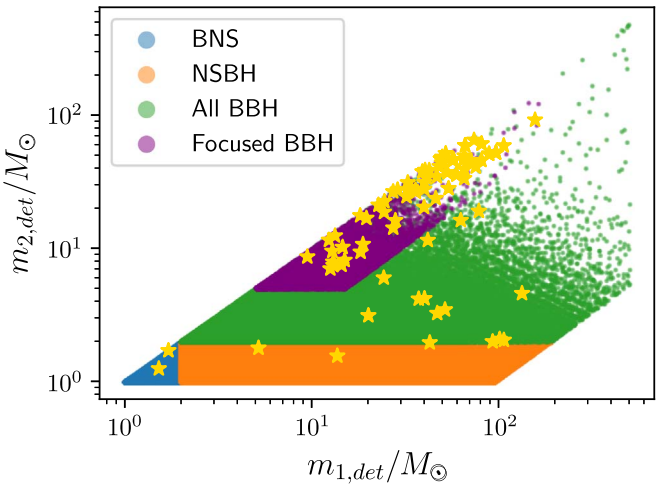

Figure 2. The bank of templates used to identify compact binary mergers in our search as a function of their detector-frame masses. The BNS (blue), NSBH (orange), BBH (green), and focused BBH (purple) regions are shown. The templates associated with an observed merger are shown with stars. Signals often have multiple templates that will produce a candidate. Here, we only show the template that produced a candidate with the lowest FAR; the parameters of the selected template can only be considered as crude point estimates of the true parameters, so they may differ significantly from the posterior estimates in Table 4.

gravitational-wave signal, we use a combination of TaylorF2 (for BNS sources; Sathyaprakash & Dhurandhar 1991; Droz et al. 1999; Blanchet 2002; Faye et al. 2012), SEOBNRv4_ROM (for BBH and NSBH; Taracchini et al. 2014; Bohé et al. 2017), and IMRPhenomD (for focused BBH; Husa et al. 2016; Khan et al. 2016).

2.3. Candidate Selection and Significance

Candidates are assigned a ranking statistic value according to their S/N, consistency with the expected signal morphology (Allen 2005; Nitz 2018), and coherence between observing detectors (Nitz et al. 2017; Davies et al. 2020). The statistical significance of multidetector candidates is assessed by comparing to empirically estimated background from artificially produced analyses. By construction, these cannot contain astrophysical sources as they are produced by time-shifting the data from one or more detectors by a constant greater than the light-travel time between detectors (Babak et al. 2013; Usman et al. 2016). This technique has been used in many past analyses (Abbott et al. 2009, 2021a, 2021g; Abadie et al. 2012; Nitz et al. 2019c; Venumadhav et al. 2019). For multidetector candidates, the estimated background distribution is used to establish the FAR of the search as a function of ranking statistic value. Candidates detected in a single detector are instead assessed against off-source observation time. In particular, we use time when both LIGO detectors are observing, which allows for confident multidetector observations to be excised from the background, minimizing potential signal contamination. To limit the effects of nonstationary noise and non-Gaussian noise transients, we further restrict our single-detector analysis to candidates that arise from either the BNS region,

focused BBH with chirp mass $\mathcal{M} < 60$, or NSBH with total mass $M < 50$. The highest mass templates of each region are the most difficult to distinguish from non-Gaussian transient noise due to their short duration.

The probability of astrophysical origin $\mathcal{P}_{\rm astro}$ is calculated using the empirically measured background and comparing to the distribution of observed ranking statistic values produced by a simulated source population as part of a two-component mixture model (Farr et al. 2015b). For the single-detector analysis, the background distribution is extrapolated using the method of Nitz et al. (2020). This is the same methodology as previously used in the 3-OGC analysis. We limit our assignment of $\mathcal{P}_{\rm astro}$ to the single-detector analyses using the method of Nitz et al. (2020) and multidetector candidates from the focused BBH region, where the vast majority of observations are found. Due to the uncertain population distribution in other regions, we do not assign a probability of astrophysical origin.

In the 3-OGC analysis, we implicitly assumed a detection prior that is flat in redshifted chirp mass (Nitz et al. 2021a) within the focused BBH region; we make a marginal improvement to this step by averaging the obtained astrophysical probability over this fiducial population scenario with the one obtained from the smoothed observed distribution of redshifted chirp masses of the high confidence observations (FAR $<$ 1 per 100 yr). Due to the broad observed distribution in chirp masses, this produces only very modest changes to the estimated astrophysical probability compared to those previously reported in 3-OGC; the primary impact is to mildly increase support for sources with $\mathcal{M} < \sim$50 in lieu of higher-mass sources. A future improvement for the assessment of marginal candidates would be to include a physical model that can simultaneously fit the population along with the foreground and background distributions.

3. Observational Results

All events identified by our search with a probability of astrophysical origin $\mathcal{P}_{\rm astro} > 0.5$ or inverse false alarm rate (IFAR) $>$ 100 yr are listed in Table 2. We report 94 events, of which 90 are BBHs, 2 originate from BNS mergers, and 2 are the results of coalescing NSBHs. The table contains information on the observational status of the three different instruments LIGO-Hanford, LIGO-Livingston, and Virgo, as well as the recovered S/N for the detectors that triggered on the event. Finally, we also provide the Global Positioning System (GPS) times, estimates of the $\mathcal{P}_{\rm astro}$ for BBH signals, and the observed IFARs.

Our search finds seven new BBH signals during O3b that pass our significance criteria and were not reported as marginal or confident observations by previous studies (Abbott et al. 2021g). These events are GW191224_043228, GW200106_134123, GW200129_114245, GW200210_005122, GW200214_223307, GW200305_084739, and GW200318_191337. In addition, three previously marginal BBH candidates from the previous 3-OGC (Nitz et al. 2021a) now pass our criteria; this is due to the updated prescription for calculating $\mathcal{P}_{\rm astro}$ (see Section 2.3). No new BNSs or NSBHs were discovered at high confidence.

The most confident new detection is GW200318_191337 with a $\mathcal{P}_{\rm astro} = 0.97$. It is detected in both LIGO-Hanford and LIGO-Livingston with S/N $\leqslant$6.2. GW200318_191337 may be the most distant observed merger with redshift $z \sim 0.84^{+0.4}_{-0.35}$. GW200129_114245 is a potential new mass ratio $\sim$2 BBH with primary mass $79.1^{+40.2}_{-37.6} M_{\odot}$. GW200129_114245 is detected by both LIGO-Hanford and LIGO-Livingston with S/N $\leqslant$6 and occurs less than 5 hr after the previous event GW200129_065458.

The results of our single-detector analysis are shown in Figure 3 for BNS, BBH, and now NSBH sources. There have now been eight mergers detected in a single detector: six BBHs, one BNS, and one NSBH. The previously reported NSBH merger GW200105_162426 (Abbott et al. 2021d) is found as a near-threshold detection in our analysis. It was observed only in LIGO-Livingston with an S/N of 13.3. LIGO-Hanford was not observing at the time. It has $\mathcal{P}_{\rm astro} \sim 0.5$, similar to GW190425, due to its wide separation from the background distribution. The assumed merger rate for similar NSBH sources is determined by the inclusion of GW200115, whose single-detector LIGO-Hanford trigger had a ranking statistic marginally larger than all collected single-detector backgrounds.

We present 30 marginal subthreshold events following the criterion $\mathcal{P}_{\rm astro} > 0.2$ or IFAR $>$0.5 yr in Table 3. The majority of these are consistent with BBH mergers except for 170722_065503 and 191219_163120, which are consistent with a BNS and an NSBH merger, respectively. In total, 11 marginal candidates were previously reported in our most recent 3-OGC; these are 151011_192749, 170425_055334, 170704_202003, 190426_053949, 190509_004120, 190530_030659, 190630_135302, 190704_104834, 190707_071722, 190808_230535, and 190821_050019. The remainder of our subthreshold candidates are included in the corresponding data release (Nitz & Kumar 2021).

We visually inspect spectrograms of the data around each marginal event to check for nonstationary behavior or an excess of non-Gaussian transient noise that could adversely affect the identified candidate. We observed excess power consistent with a blip glitch (Cabero et al. 2019) in several cases at off-source times. In a few other events we observe slight deviations in power from the expected stationary Gaussian noise in the frequency range 60–110 Hz, e.g., in the Hanford data a few seconds before the time of events (e.g., 200102_095606 or 200310_090144). Further investigation would be required to determine if potential candidates could be adversely affected in these cases.

Our results are otherwise broadly consistent with those of the recently published GWTC-3 catalog (Abbott et al. 2021g). There are eight events reported in GWTC-3 that do not pass our candidate threshold. These are GW191103_012549, GW191113_071753, GW191219_163120, GW200208_222617, GW200210_092254, GW200220_061928, GW200220_124850, and GW200322_091133. Both potential new NSBH candidates GW191219_163120 and GW200210_092254 from GWTC-3 are not assigned high confidence by our search. GW191219_163120 and GW200220_124850 are detected as near-threshold triggers with a $\mathcal{P}_{\rm astro} > 0.2$ or IFAR $>$ 0.5 yr. All other events are assigned a lower significance. We expect these small differences in the population of near-threshold events are consistent with differing analysis choices. We note that our candidate threshold is marginally more conservative; GWTC-3 includes candidates with $\mathcal{P}_{\rm astro} > 0.5$ in any of several analyses (Abbott et al. 2021g).

3.1. Binary Source Parameters

In order to infer the properties of the observed compact binary mergers, we use PyCBC inference (Biwer et al. 2019) to perform Bayesian parameter estimation with the standard

Table 2
Gravitational-wave Observations from the Full Search on Data from O1 to O3 with $\mathcal{P}_{\rm astro} > 0.5$ or IFAR > 100 yr, Sorted by Observation Time

	Event	GPS Time	Observing	Triggered	$\mathcal{P}_{\rm astro}$	IFAR (yr)	$\rho_{\rm H}$	$\rho_{\rm L}$	$\rho_{\rm V}$
1	GW150914_095045	1126259462.43	HL	HL	1.00	>100	19.9	13.0	⋯
2	GW151012_095443	1128678900.45	HL	HL	1.00	>100	6.9	6.6	⋯
3	GW151226_033853	1135136350.65	HL	HL	1.00	>100	10.5	7.4	⋯
4	GW170104_101158	1167559936.60	HL	HL	1.00	>100	8.9	9.6	⋯
5	GW170121_212536	1169069154.58	HL	HL	1.00	16	5.2	8.9	⋯
6	GW170202_135657	1170079035.73	HL	HL	0.86	0.50	5.4	6.2	⋯
7	GW170304_163753	1172680691.37	HL	HL	0.74	0.25	4.6	7.0	⋯
8	GW170403_230611	1175295989.23	HL	HL	0.72	0.25	5.2	5.5	⋯
9	GW170608_020116	1180922494.49	HL	HL	1.00	>100	12.4	9.0	⋯
10	GW170727_010430	1185152688.03	HL	HL	1.00	71	4.7	7.5	⋯
11	GW170729_185629	1185389807.32	HL	HL	1.00	28	7.5	6.9	⋯
12	GW170809_082821	1186302519.75	HLV	HL	1.00	>100	6.7	10.7	⋯
13	GW170814_103043	1186741861.53	HLV	HL	1.00	>100	9.2	13.7	⋯
14	GW170817_124104	1187008882.45	HLV	HL	⋯	>100	18.3	25.5	⋯
15	GW170818_022509	1187058327.08	HLV	HL	1.00	5.26	4.5	9.6	⋯
16	GW170823_131358	1187529256.52	HL	HL	1.00	>100	6.6	9.1	⋯
17	GW190404_142514	1238423132.99	HL	HL	0.50	0.02	5.1	5.9	⋯
18	GW190408_181802	1238782700.28	HLV	HL	1.00	>100	9.2	10.3	⋯
19	GW190412_053044	1239082262.17	HLV	HL	1.00	>100	8.2	14.9	⋯
20	GW190413_052954	1239168612.50	HLV	HL	1.00	1.45	5.2	6.7	⋯
21	GW190413_134308	1239198206.74	HLV	HL	1.00	6.39	5.4	7.8	⋯
22	GW190421_213856	1239917954.25	HL	HL	1.00	>100	7.9	6.3	⋯
23	GW190424_180648	1240164426.14	L	L	0.53	⋯	⋯	9.9	⋯
24	GW190425_081805	1240215503.02	LV	L	0.50	⋯	⋯	11.9	⋯
25	GW190427_180650	1240423628.68	HLV	HL	0.53	0.02	5.8	6.8	⋯
26	GW190503_185404	1240944862.29	HLV	HL	1.00	>100	9.1	7.6	⋯
27	GW190512_180714	1241719652.42	HLV	HL	1.00	>100	5.9	10.8	⋯
28	GW190513_205428	1241816086.74	HLV	HLV	1.00	>100	8.8	7.7	4.0
29	GW190514_065416	1241852074.85	HL	HL	0.82	0.19	6.1	5.3	⋯
30	GW190517_055101	1242107479.83	HLV	HL	1.00	66	6.8	7.9	⋯
31	GW190519_153544	1242315362.38	HLV	HL	1.00	>100	7.8	9.3	⋯
32	GW190521_030229	1242442967.44	HLV	HL	1.00	>100	8.4	12.0	⋯
33	GW190521_074359	1242459857.47	HL	HL	1.00	>100	12.1	21.0	⋯
34	GW190527_092055	1242984073.79	HL	HL	0.94	0.37	5.0	7.0	⋯
35	GW190602_175927	1243533585.10	HLV	HL	1.00	>100	6.2	10.8	⋯
36	GW190620_030421	1245035079.31	LV	L	0.73	⋯	⋯	11.2	⋯
37	GW190630_185205	1245955943.18	LV	LV	1.00	0.18	⋯	14.7	4.0
38	GW190701_203306	1246048404.58	HLV	HLV	1.00	0.13	6.0	8.9	5.7
39	GW190706_222641	1246487219.33	HLV	HL	1.00	>100	9.4	8.6	⋯
40	GW190707_093326	1246527224.17	HL	HL	1.00	>100	7.9	9.6	⋯
41	GW190708_232457	1246663515.38	LV	L	0.73	⋯	⋯	12.6	⋯
42	GW190719_215514	1247608532.92	HL	HL	0.92	0.25	5.6	5.7	⋯
43	GW190720_000836	1247616534.71	HLV	HL	1.00	>100	6.8	7.7	⋯
44	GW190725_174728	1248112066.46	HLV	HL	0.96	0.41	5.4	7.3	⋯
45	GW190727_060333	1248242631.98	HLV	HL	1.00	>100	7.9	8.1	⋯
46	GW190728_064510	1248331528.53	HLV	HL	1.00	>100	7.5	10.6	⋯
47	GW190731_140936	1248617394.64	HL	HL	0.92	0.43	5.2	6.0	⋯
48	GW190803_022701	1248834439.88	HLV	HL	1.00	2.40	5.6	6.7	⋯
49	GW190805_105432	1249037690.78	HL	HL	0.51	0.02	4.8	6.5	⋯
50	GW190814_211039	1249852257.01	HLV	HL	⋯	>100	11.0	21.1	⋯
51	GW190828_063405	1251009263.76	HLV	HL	1.00	>100	10.3	11.2	⋯
52	GW190828_065509	1251010527.89	HLV	HL	1.00	>100	7.3	7.4	⋯
53	GW190910_112807	1252150105.32	LV	L	0.77	⋯	⋯	13.4	⋯
54	GW190915_235702	1252627040.70	HLV	HL	1.00	>100	9.0	8.6	⋯
55	GW190916_200658	1252699636.90	HLV	HL	0.90	0.22	4.9	5.9	⋯
56	GW190924_021846	1253326744.84	HLV	HL	1.00	>100	6.7	10.8	⋯
57	GW190925_232845	1253489343.12	HV	HV	1.00	>100	8.2	⋯	5.4
58	GW190926_050336	1253509434.07	HLV	HL	0.92	0.27	5.4	5.6	⋯
59	GW190929_012149	1253755327.50	HLV	HL	0.99	3.08	5.8	7.4	⋯
60	GW190930_133541	1253885759.24	HL	HL	1.00	>100	6.7	7.4	⋯
61	GW191105_143521	1256999739.93	HLV	HL	1.00	>100	6.0	7.7	⋯
62	GW191109_010717	1257296855.21	HL	HL	1.00	>100	9.5	13.0	⋯
63	GW191126_115259	1258804397.63	HL	HL	1.00	4.86	5.8	6.7	⋯
64	GW191127_050227	1258866165.55	HLV	HL	0.99	0.15	5.4	6.4	⋯

Table 2
(Continued)

	Event	GPS Time	Observing	Triggered	$\mathcal{P}_{\rm astro}$	IFAR (yr)	$\rho_{\rm H}$	$\rho_{\rm L}$	$\rho_{\rm V}$
65	GW191129_134029	1259070047.18	HL	HL	1.00	>100	6.9	8.0	···
66	GW191204_110529	1259492747.54	HL	HL	0.99	1.59	5.0	7.7	···
67	GW191204_171526	1259514944.09	HL	HL	1.00	>100	9.2	13.3	···
68	GW191215_223052	1260484270.33	HLV	HL	1.00	>100	7.4	7.8	···
69	GW191216_213338	1260567236.48	HV	HV	1.00	55	17.5	···	5.5
70	GW191222_033537	1261020955.12	HL	HL	1.00	>100	8.6	8.2	···
71	**GW191224_043228**	1261197166.15	HLV	HL	0.87	0.13	5.0	6.8	···
72	GW191230_180458	1261764316.40	HLV	HL	1.00	>100	7.5	6.7	···
73	GW200105_162426	1262276684.06	LV	L	0.50	···	···	13.3	···
74	**GW200106_134123**	1262353301.93	HLV	HL	0.69	0.06	5.2	5.2	···
75	GW200112_155838	1262879936.09	LV	L	0.78	···	···	18.6	···
76	GW200115_042309	1263097407.74	HLV	HL	···	>100	6.5	8.5	···
77	GW200128_022011	1264213229.90	HL	HL	1.00	>100	7.0	7.0	···
78	GW200129_065458	1264316116.42	HLV	HV	1.00	>100	14.6	···	7.0
79	**GW200129_114245**	1264333383.11	HLV	HL	0.53	0.04	5.1	6.0	···
80	GW200202_154313	1264693411.56	HLV	HL	1.00	6.05	5.1	9.6	···
81	GW200208_130117	1265202095.95	HLV	HLV	1.00	>100	6.8	6.9	4.5
82	GW200209_085452	1265273710.17	HLV	HL	0.99	1.10	7.1	5.9	···
83	**GW200210_005122**	1265331100.74	HLV	HL	0.74	0.04	5.4	6.3	···
84	**GW200214_223307**	1265754805.00	HLV	HL	0.72	0.08	5.2	5.2	···
85	GW200216_220804	1265926102.89	HLV	HL	0.78	0.09	6.6	5.6	···
86	GW200219_094415	1266140673.20	HLV	HL	1.00	22	5.7	8.0	···
87	GW200224_222234	1266618172.40	HLV	HL	1.00	>100	12.6	13.0	···
88	GW200225_060421	1266645879.40	HL	HL	1.00	>100	9.6	7.8	···
89	GW200302_015811	1267149509.52	HV	H	0.66	···	10.5	···	···
90	**GW200305_084739**	1267433277.08	HLV	HL	0.59	0.02	4.5	6.1	···
91	GW200306_093714	1267522652.12	HL	HL	0.51	0.02	5.5	5.9	···
92	GW200311_115853	1267963151.39	HLV	HLV	1.00	>100	12.0	9.9	6.7
93	GW200316_215756	1268431094.16	HLV	HL	1.00	22	5.4	7.8	···
94	**GW200318_191337**	1268594035.14	HLV	HL	0.97	0.50	4.8	6.2	···

Note. We list the GPS time for each event alongside information on the observational status of the three observatories LIGO-Hanford (H), LIGO-Livingston (L), and Virgo (V). We also list the detectors for which our search triggered and the corresponding recovered S/Ns (ρ). For some events, where multiple detectors are operational, the search does not trigger for all observatories. This is caused by requiring consistency of the triggers between detectors and triggers in individual detectors needing to exceed the S/N threshold. For multidetector events we provide the IFAR at the associated ranking statistic for the event. The probability of astrophysical origin is estimated for all events detected by the focused BBH search and from the single-detector analyses. Events reported here for the first time are set in bold font.

likelihood assuming the detector noise to be stationary, Gaussian, and uncorrelated between the detectors. The parameter estimation results for a total of 94 events are summarized in Figure 4 and Table 4.

For estimating the source parameters of the BBHs, we use IMRPhenomXPHM (LALSuite 2020; Pratten et al. 2021), which models precessing binaries and includes higher-order modes. For the two NSBH observations, we use the IMRPhenomNSBH (Thompson et al. 2020) waveform that models a nonprecessing NSBH with the neutron star mass $m_{\rm NS} \leqslant 3M_{\odot}$, tidal deformability $\Lambda \in [0, 5000]$, and a mass ratio no higher than 100 (LALSuite 2020). For the BNS mergers, we use the IMRPhenomD_NRTidal waveform model (Husa et al. 2016; Khan et al. 2016; Dietrich et al. 2017, 2019; LALSuite 2020). This model includes the two tidal deformabilities, Λ_1 and Λ_2 of the two components, which characterize the neutron star equation of state. A dynamical nested sampler *dynesty* (Speagle 2020) is used to sample over the intrinsic parameters mass $m_{1,2}$ and spin $\boldsymbol{s}_{1,2}$ (in the case of BNS, also tidal deformabilities $\Lambda_{1,2}$; in the case of NSBH, we include the NS tidal deformability Λ_2) and over extrinsic parameters luminosity distance d_L, inclination angle ι, polarization angle Ψ, R.A. α, decl. δ, coalescence time t_c, and phase ϕ_c. For BBH sources, the likelihood is marginalized numerically over Ψ, while for BNS and NSBH sources, it is analytically marginalized over ϕ_c.

We also take into account the effect of calibration uncertainties in amplitude and frequency on the parameter estimation of each event. We use the calibration uncertainty envelopes obtained from the GWOSC for previously known mergers (Vallisneri et al. 2015). For the new BBH events, we use the calibration uncertainty envelope from the nearest available time, assuming the calibration envelopes do not change rapidly. The calibration errors in amplitude and phase of the data in each detector are described by frequency-dependent splines (Farr et al. 2015a) whose parameters are directly sampled over in our analysis. We find that the estimation of intrinsic parameters is not significantly affected by the calibration uncertainties.

The priors for the intrinsic and extrinsic parameters and the power spectral density estimation methods, as well as the sampler settings, are broadly consistent with those used in the 3-OGC

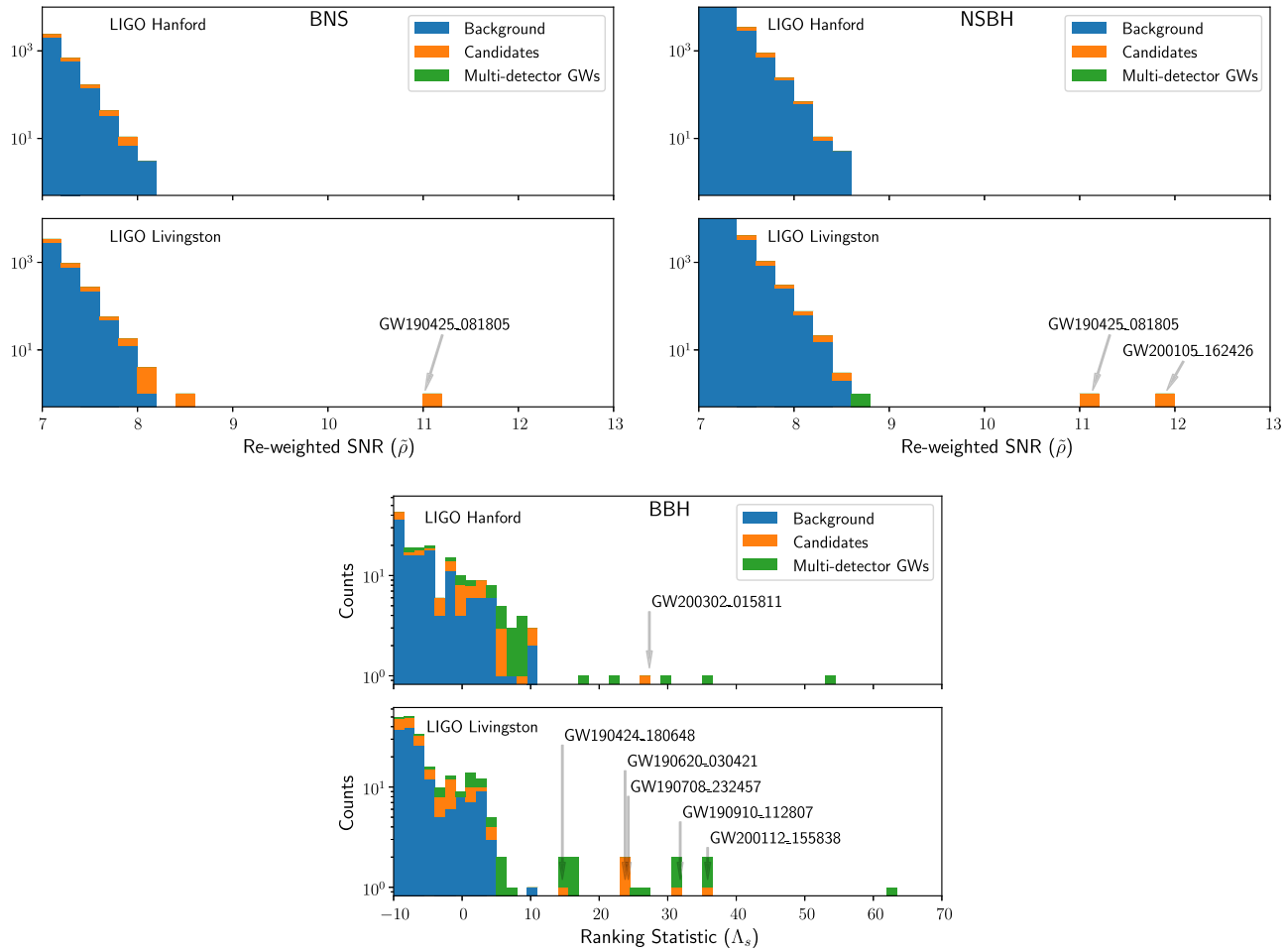

Figure 3. The stacked distributions of single-detector triggered candidates observed during O3 when a single LIGO observatory was operating (orange), our selected background (blue), and for comparison the distribution of gravitational-wave mergers observed by the multidetector analysis (green) as a function of the ranking statistic. Results from the BNS (top left), NSBH (top right), and BBH (bottom) analyses are shown. The method of Nitz et al. 2020 is used to extrapolate the background distribution and estimate the probability of astrophysical origin. The BBH analysis uses the statistic λ_s (Nitz et al. 2020) while the others use a reweighted S/N statistic (Babak et al. 2013; Nitz et al. 2019c). GW190425 appears in both the BNS and NSBH analyses as candidates were produced from both regions.

analysis (Nitz et al. 2021a). For the BBH events, uniform priors on source-frame component masses and merger time are used. For the spins, we use uniform priors for the magnitude of the spin and isotropic priors for the orientation. The distance prior is assumed to be uniform in comoving volume assuming a flat ΛCDM cosmological model (Ade et al. 2016). For the rest of the extrinsic parameters, we consider an isotropic prior distribution in the sky localization and binary orientation.

For the two NSBH systems, the prior on the tidal deformability of the neutron star is considered to be uniform in the range [0, 5000]. Other prior distributions are the same as BBH events except that the NS spin magnitude is uniform in [0, 0.05] and the BH is uniform in [0, 0.5]. This latter range is chosen based on the parameter space where the waveform model is valid (Thompson et al. 2020; Abbott et al. 2021d).

In the case of BNS mergers, we use the same prior distributions for the component masses, comoving volume, merger time, and orientation as used in estimating the BBH parameters. However, for GW170817_124104, we fix the sky location to that from the observed electromagnetic counterpart, $\alpha = 3.446$ and $\delta = -0.408$ (Abbott et al. 2017b). The spin magnitudes for the two components are uniform in the range [0, 0.05]. We also vary the tidal deformability parameters of the NS components Λ_1 and Λ_2 independently in the range [0, 5000].

3.2. Binary Black Holes

A total of 90 BBH mergers have now been observed that pass our significance threshold. The growing population will eventually enable distinguishing possible formation channels and the potential contribution from each (Talbot & Thrane 2018; Abbott et al. 2019b, 2021b, 2021h; Roulet et al. 2020). Notable features expected of the BBH population were the lower (Gupta et al. 2020; Zevin et al. 2020) and upper (Fishbach & Holz 2020; Edelman et al. 2021) mass gaps; the former is an observational expectation from X-ray binaries (Özel et al. 1918; Bailyn et al. 1998; Farr et al. 2011), while the latter is expected due to pair-instability supernovae (Woosley 2017; Marchant et al. 2019; Stevenson et al. 2019; van Son et al. 2020).

Several events have components plausibly within the lower mass gap; notably GW190427_180650, GW190725_174728, GW190924_021846, GW190930_133541, GW200210_005122, and GW200316_215756 have posterior support for the secondary mass below 5 $M_\odot$. GW190814, however, has secondary mass well constrained to be within this region with secondary mass $2.6^{+0.2}_{-0.1} M_\odot$. The upper mass gap is expected to occur at ∼50–120 $M_\odot$(Yoshida et al. 2016; Belczynski et al. 2016; Woosley 2017, 2017; Marchant et al. 2019; Stevenson et al. 2019; van Son et al. 2020). Several detections, including

Table 3
The Selection of Subthreshold Candidates with $\mathcal{P}_{\rm astro} > 0.2$ or IFAR >0.5 from the Full Search of O1–O3 data

	Event	GPS Time	Observing	Triggered	$\mathcal{P}_{\rm astro}$	IFAR	ρ_H	ρ_L	ρ_V	$m_{1,\rm det}/M_\odot$	$m_{2,\rm det}/M_\odot$	$\chi_{\rm eff}$
1	151011_192749	1128626886.60	HL	HL	0.24	0.02	4.7	6.8	⋯	33.5	65.6	0.1
2	170425_055334	1177134832.19	HL	HL	0.37	0.07	5.3	5.8	⋯	46.1	65.0	0.1
3	170623_234223	1182296561.37	HL	HL	0.23	0.02	5.5	5.8	⋯	18.2	14.4	0.1
4	170704_202003	1183234821.62	HL	HL	0.43	0.05	5.1	6.5	⋯	10.0	13.2	−0.0
5	170722_065503	1184741721.32	HL	HL	⋯	0.89	5.0	7.3	⋯	1.7	1.3	−0.0
6	190424_081138	1240128716.76	HLV	HL	0.25	0.01	5.1	5.5	⋯	28.4	35.1	0.0
7	190426_053949	1240292407.21	HLV	HL	0.40	0.01	5.2	6.1	⋯	20.7	20.0	0.2
8	190509_004120	1241397698.79	HLV	HL	0.37	0.01	4.7	6.2	⋯	30.1	28.2	−0.0
9	190519_231324	1242342822.07	HLV	HL	0.26	0.01	5.6	5.9	⋯	6.6	8.7	−0.0
10	190530_030659	1243220837.97	HLV	HL	0.44	0.01	5.2	5.8	⋯	26.3	45.4	0.2
11	190630_135302	1245938000.49	HL	HL	0.26	0.01	5.1	5.8	⋯	32.6	19.2	0.0
12	190704_104834	1246272532.92	HLV	HL	0.27	0.01	7.0	5.5	⋯	5.0	5.4	0.1
13	190707_071722	1246519060.10	HLV	HL	0.32	0.01	6.0	5.7	⋯	10.7	14.1	0.0
14	190731_105943	1248606001.71	HLV	HV	0.29	0.01	6.4	⋯	5.2	39.1	37.6	−0.0
15	190808_230535	1249340753.59	HLV	HL	0.41	0.01	5.0	6.5	⋯	13.6	13.6	0.2
16	190821_050019	1250398837.88	HLV	HL	0.31	0.01	5.2	5.6	⋯	26.8	17.0	−0.1
17	191102_232120	1256772098.02	HLV	HL	0.22	0.01	4.9	5.9	⋯	32.0	23.1	−0.0
18	191116_022801	1257906499.42	HLV	HL	0.22	0.00	5.2	6.4	⋯	12.2	7.5	0.2
19	191122_214924	1258494582.97	HLV	HL	0.24	0.01	4.2	7.3	⋯	59.0	106.7	0.2
20	191201_054144	1259214122.47	HV	HV	⋯	0.66	7.1	⋯	5.8	3.0	9.0	−0.4
21	191208_080334	1259827432.84	HLV	HL	0.23	0.01	6.0	4.8	⋯	26.7	50.1	−0.1
22	191219_163120	1260808298.45	HLV	HL	⋯	0.31	5.0	7.4	⋯	1.7	22.7	−0.5
23	200102_095606	1261994184.05	HLV	HV	⋯	0.47	8.9	⋯	4.1	123.3	77.2	0.2
24	200116_082400	1263198258.97	HLV	HL	0.21	0.01	4.9	5.8	⋯	20.7	16.7	−0.1
25	200122_161511	1263744929.34	HL	HL	0.27	0.01	5.7	5.7	⋯	6.6	13.1	0.0
26	200205_141704	1264947442.84	HL	HL	0.23	0.01	5.5	5.9	⋯	10.3	11.1	0.2
27	200220_124850	1266238148.15	HL	HL	0.43	0.03	6.0	5.3	⋯	49.4	65.7	−0.1
28	200301_211019	1267132237.66	HL	HL	0.43	0.02	5.5	5.9	⋯	31.8	17.8	−0.0
29	200304_182240	1267381378.62	HL	HL	0.28	0.01	4.6	5.7	⋯	44.3	28.4	−0.1
30	200310_090144	1267866122.76	HL	HL	0.43	0.02	5.2	6.1	⋯	11.9	6.1	0.0

Note. Candidates are sorted by observation time. The complete set of subthreshold candidates is available in the data release and includes a selection of full parameter estimates. Here we show the detector-frame (redshifted) parameters of the template that triggered on the candidate, along with the reported S/Ns (ρ) from each detector.

GW190521 (Abbott et al. 2020c), have primary masses within this range. One explanation is that these may be second-generation mergers (Rodriguez et al. 2019; Kimball et al. 2020; Gerosa & Fishbach 2021). Other exceptional observations include the high-mass-ratio GW190814 merger ($q \sim 9$); several proposals exist to explain its formation (Carr et al. 2021; Clesse & Garcia-Bellido 2020; Lu et al. 2020; Olejak et al. 2020; Liu & Lai 2021).

The observed distribution of source parameters (e.g., masses and spins) and redshift distribution from a large catalog of compact binary mergers can be used to constrain the population models that predict intrinsic source distribution as well as the rate of mergers (Abbott et al. 2019b, 2021c, 2021h; Zhu et al. 2022; Roulet et al. 2021). In Figure 5, we show the distribution of component masses obtained from stacking all the posteriors marginalized over all other parameters, with and without taking into account the zeroth order selection effect that arises due to the loudness of the signal as a function of source parameters. To infer the source population, we use the same method as in the 3-OGC analysis (Nitz & Capano 2021). We combine the posterior samples from each event to obtain large mass samples. We assume the same priors that we used in the parameter estimation. To account for the loudness of the signal, we estimate the comoving volume corresponding to the "horizon distance" of a posterior sample and reassign each sample a weight proportional to the inverse of the comoving volume. The horizon distance is defined as the maximum distance an optimally oriented source can be detected.

3.3. BBH Population and Merger Rate

We use the posterior samples from the individual source parameter estimation study to infer the distributions of source-frame masses and redshifts for BBHs. The intrinsic distribution of BBH mergers can be parametrized in terms of the "hyper-parameters" $\Theta^{\rm pop}$ of a population model (Abbott et al. 2021c, 2021h; Thrane & Talbot 2020; Vitale et al. 2020). The hyper-parameters describe the shape of the distribution in observed parameters θ such as masses, spins, redshift, etc. To compare the inferred BBH distribution for masses and redshift with other catalogs, we demonstrate using models that were also employed in GWTC-3 studies (Abbott et al. 2021h). The sensitivity of our search is estimated by analyzing a simulated population that is injected throughout the O1–O3 data. Our fiducial population includes sources that extend up to a total mass of 300 $M_\odot$ and maximum mass ratio q of 30 with constraints on individual component masses to be between 2 and 150$M_\odot$. In the GWTC-3 analysis, the search sensitivity is estimated semianalytically for O1+O2 and with direct search performance for O3 (Collaboration et al. 2021a, 2021b; Abbott et al. 2021h) using a fiducial BBH population set with

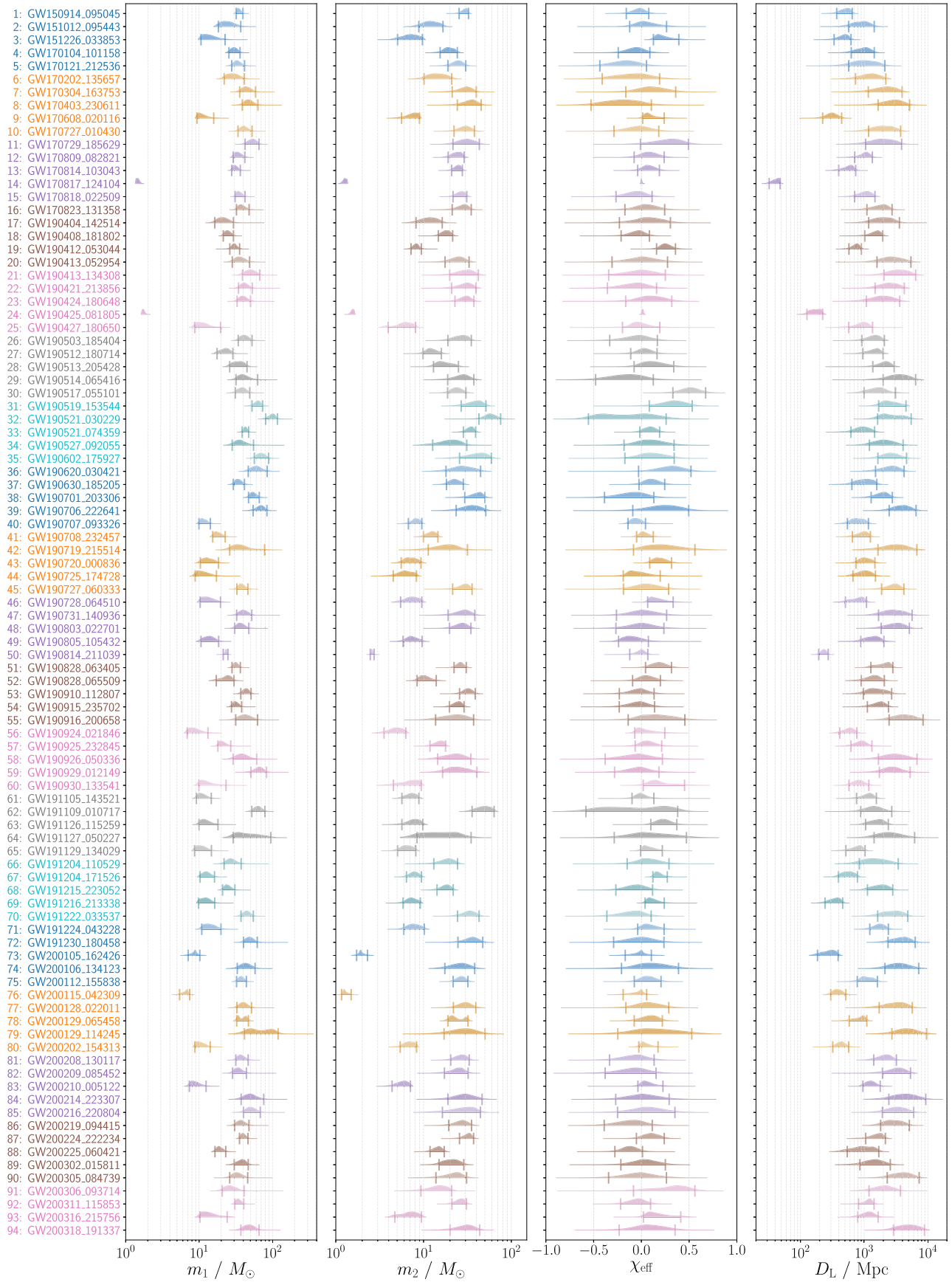

Figure 4. The marginalized distributions for component masses m_1, m_2, the effective spin $\chi_{\rm eff}$, and the luminosity distance $D_{\rm L}$ for all events that pass our detection criteria in 4-OGC (fourth Gravitational-wave Catalog). The fifth and ninety-fifth quantile values are marked with a bar. Different colors are used to aid associating each event with its posterior estimates.

Table 4
Bayesian Parameter Estimates for All 94 Detections from O1 to O3 Scientific Runs, with the Ones Reported Here for the First Time in Bold

	Event	$m_1/M_\odot$	$m_2/M_\odot$	$\mathcal{M}/M_\odot$	q	$\chi_{\rm eff}$	$D_{\rm L}$/Mpc	z	$M_{\rm f}/M_\odot$	χ_f	S/N
1	GW150914_095045	$34.9^{+4.7}_{-2.9}$	$29.7^{+2.8}_{-4.2}$	$27.9^{+1.4}_{-1.3}$	$1.2^{+0.4}_{-0.2}$	$-0.03^{+0.1}_{-0.13}$	525^{+124}_{-154}	$0.11^{+0.02}_{-0.03}$	$61.6^{+2.9}_{-2.6}$	$0.69^{+0.05}_{-0.04}$	24.0
2	GW151012_095443	$25.2^{+11.8}_{-6.9}$	$12.5^{+4.1}_{-3.7}$	$15.1^{+1.3}_{-1.0}$	$2.0^{+2.1}_{-0.9}$	$0.04^{+0.22}_{-0.16}$	976^{+464}_{-406}	$0.19^{+0.08}_{-0.08}$	$36.4^{+8.5}_{-4.2}$	$0.65^{+0.09}_{-0.09}$	10.2
3	GW151226_033853	$14.2^{+8.4}_{-3.6}$	$7.4^{+2.3}_{-2.3}$	$8.8^{+0.2}_{-0.2}$	$1.9^{+2.5}_{-0.8}$	$0.21^{+0.18}_{-0.08}$	494^{+129}_{-157}	$0.1^{+0.02}_{-0.03}$	$20.6^{+6.3}_{-1.5}$	$0.75^{+0.1}_{-0.04}$	13.5
4	GW170104_101158	$30.2^{+5.9}_{-4.7}$	$19.7^{+4.5}_{-4.3}$	$21.1^{+1.8}_{-1.6}$	$1.5^{+0.7}_{-0.5}$	$-0.06^{+0.15}_{-0.18}$	1032^{+409}_{-404}	$0.2^{+0.07}_{-0.07}$	$48.0^{+3.7}_{-3.3}$	$0.66^{+0.07}_{-0.09}$	13.8
5	GW170121_212536	$33.4^{+8.2}_{-5.6}$	$24.8^{+5.4}_{-5.9}$	$24.9^{+3.4}_{-3.1}$	$1.3^{+0.7}_{-0.3}$	$-0.17^{+0.22}_{-0.26}$	1204^{+913}_{-632}	$0.23^{+0.15}_{-0.11}$	$56.0^{+7.5}_{-6.7}$	$0.64^{+0.09}_{-0.11}$	11.0
6	GW170202_135657	$29.7^{+11.7}_{-7.7}$	$15.0^{+6.0}_{-4.9}$	$17.9^{+2.7}_{-1.9}$	$2.0^{+2.0}_{-0.9}$	$-0.09^{+0.28}_{-0.32}$	1379^{+811}_{-645}	$0.26^{+0.13}_{-0.11}$	$43.5^{+8.0}_{-5.5}$	$0.61^{+0.13}_{-0.15}$	9.1
7	GW170304_163753	$44.8^{+14.0}_{-9.1}$	$30.9^{+8.9}_{-9.8}$	$32.0^{+6.2}_{-5.2}$	$1.4^{+1.1}_{-0.4}$	$0.1^{+0.26}_{-0.27}$	2458^{+1496}_{-1295}	$0.43^{+0.21}_{-0.21}$	$72.3^{+14.0}_{-10.6}$	$0.73^{+0.1}_{-0.12}$	9.0
8	GW170403_230611	$48.3^{+15.0}_{-9.5}$	$35.2^{+10.1}_{-10.9}$	$35.4^{+7.7}_{-6.0}$	$1.3^{+1.0}_{-0.3}$	$-0.2^{+0.3}_{-0.33}$	3208^{+1975}_{-1551}	$0.54^{+0.26}_{-0.23}$	$80.1^{+16.8}_{-12.6}$	$0.62^{+0.12}_{-0.14}$	8.0
9	GW170608_020116	$11.0^{+4.8}_{-1.6}$	$7.7^{+1.3}_{-2.1}$	$8.0^{+0.2}_{-0.2}$	$1.4^{+1.4}_{-0.4}$	$0.08^{+0.16}_{-0.06}$	322^{+122}_{-99}	$0.07^{+0.02}_{-0.02}$	$17.9^{+2.8}_{-0.6}$	$0.7^{+0.05}_{-0.04}$	15.4
10	GW170727_010430	$41.5^{+11.1}_{-7.6}$	$30.2^{+7.7}_{-8.0}$	$30.5^{+5.3}_{-4.2}$	$1.3^{+0.8}_{-0.3}$	$-0.03^{+0.21}_{-0.26}$	2316^{+1433}_{-1141}	$0.41^{+0.2}_{-0.18}$	$68.6^{+11.4}_{-9.1}$	$0.68^{+0.09}_{-0.1}$	9.0
11	GW170729_185629	$53.8^{+11.6}_{-11.5}$	$31.9^{+11.3}_{-10.2}$	$35.3^{+7.1}_{-5.9}$	$1.7^{+1.1}_{-0.6}$	$0.28^{+0.21}_{-0.29}$	2290^{+1590}_{-1234}	$0.41^{+0.23}_{-0.2}$	$81.0^{+13.9}_{-11.0}$	$0.79^{+0.08}_{-0.18}$	11.0
12	GW170809_082821	$34.2^{+7.9}_{-5.1}$	$24.4^{+4.6}_{-5.3}$	$24.9^{+2.0}_{-1.5}$	$1.4^{+0.8}_{-0.3}$	$0.08^{+0.16}_{-0.16}$	1064^{+281}_{-352}	$0.21^{+0.05}_{-0.06}$	$55.9^{+4.6}_{-3.4}$	$0.71^{+0.08}_{-0.08}$	12.7
13	GW170814_103043	$31.2^{+5.3}_{-3.4}$	$24.7^{+3.0}_{-3.8}$	$24.0^{+1.3}_{-1.0}$	$1.3^{+0.5}_{-0.2}$	$0.07^{+0.12}_{-0.11}$	595^{+142}_{-197}	$0.12^{+0.03}_{-0.04}$	$53.2^{+2.8}_{-2.4}$	$0.71^{+0.06}_{-0.05}$	17.7
14	GW170817_124104	$1.5^{+0.1}_{-0.1}$	$1.3^{+0.1}_{-0.1}$	$1.186^{+0.002}_{-0.002}$	$1.2^{+0.2}_{-0.1}$	$0.0^{+0.01}_{-0.01}$	42^{+6}_{-9}	$0.01^{+0.0}_{-0.0}$	…	…	32.7
15	GW170818_022509	$35.3^{+6.9}_{-4.4}$	$26.8^{+4.2}_{-5.1}$	$26.7^{+1.9}_{-1.8}$	$1.3^{+0.6}_{-0.3}$	$-0.06^{+0.17}_{-0.21}$	1094^{+386}_{-385}	$0.21^{+0.07}_{-0.07}$	$59.6^{+4.2}_{-3.7}$	$0.68^{+0.07}_{-0.08}$	12.0
16	GW170823_131358	$38.2^{+9.8}_{-5.9}$	$28.7^{+6.2}_{-7.5}$	$28.5^{+4.1}_{-3.1}$	$1.3^{+0.8}_{-0.3}$	$0.05^{+0.2}_{-0.22}$	1954^{+794}_{-848}	$0.36^{+0.12}_{-0.14}$	$63.7^{+8.7}_{-6.3}$	$0.71^{+0.08}_{-0.09}$	11.7
17	GW190404_142514	$21.6^{+7.8}_{-5.3}$	$12.1^{+4.2}_{-3.9}$	$13.8^{+2.2}_{-1.9}$	$1.8^{+1.6}_{-0.7}$	$0.07^{+0.24}_{-0.3}$	2225^{+1358}_{-1046}	$0.4^{+0.19}_{-0.17}$	$32.6^{+5.5}_{-4.6}$	$0.68^{+0.11}_{-0.18}$	8.1
18	GW190408_181802	$24.7^{+4.6}_{-3.4}$	$18.2^{+3.2}_{-3.5}$	$18.3^{+1.6}_{-1.1}$	$1.4^{+0.6}_{-0.3}$	$-0.04^{+0.13}_{-0.17}$	1572^{+391}_{-549}	$0.3^{+0.06}_{-0.09}$	$41.1^{+3.3}_{-2.6}$	$0.67^{+0.05}_{-0.07}$	14.4
19	GW190412_053044	$30.3^{+5.3}_{-4.1}$	$8.3^{+1.2}_{-1.1}$	$13.2^{+0.4}_{-0.3}$	$3.7^{+1.3}_{-0.9}$	$0.25^{+0.1}_{-0.09}$	758^{+148}_{-181}	$0.15^{+0.03}_{-0.03}$	$37.5^{+4.4}_{-3.2}$	$0.67^{+0.05}_{-0.04}$	19.3
20	GW190413_052954	$36.5^{+12.2}_{-8.2}$	$25.3^{+7.7}_{-7.7}$	$26.1^{+5.5}_{-4.6}$	$1.4^{+1.1}_{-0.4}$	$0.01^{+0.27}_{-0.32}$	3104^{+2334}_{-1511}	$0.53^{+0.31}_{-0.23}$	$59.3^{+12.0}_{-10.0}$	$0.68^{+0.11}_{-0.13}$	8.9
21	GW190413_134308	$51.3^{+15.6}_{-12.3}$	$31.2^{+10.8}_{-11.4}$	$34.0^{+7.1}_{-6.1}$	$1.6^{+1.5}_{-0.6}$	$-0.01^{+0.26}_{-0.33}$	3955^{+2501}_{-1907}	$0.64^{+0.32}_{-0.27}$	$79.1^{+15.0}_{-12.6}$	$0.68^{+0.11}_{-0.16}$	10.3
22	GW190421_213856	$42.0^{+11.0}_{-7.5}$	$31.1^{+8.4}_{-10.2}$	$30.9^{+5.9}_{-4.9}$	$1.3^{+1.0}_{-0.3}$	$-0.07^{+0.23}_{-0.29}$	2734^{+1542}_{-1247}	$0.47^{+0.21}_{-0.19}$	$69.7^{+12.2}_{-9.6}$	$0.67^{+0.09}_{-0.13}$	10.1
23	GW190424_180648	$40.1^{+10.2}_{-7.1}$	$30.6^{+6.9}_{-7.8}$	$30.2^{+5.0}_{-4.3}$	$1.3^{+0.7}_{-0.3}$	$0.1^{+0.22}_{-0.26}$	2208^{+1419}_{-1125}	$0.4^{+0.2}_{-0.18}$	$67.2^{+10.9}_{-8.8}$	$0.73^{+0.09}_{-0.1}$	10.5
24	GW190425_081805	$1.7^{+0.1}_{-0.1}$	$1.6^{+0.1}_{-0.1}$	$1.431^{+0.015}_{-0.013}$	$1.1^{+0.2}_{-0.1}$	$0.01^{+0.01}_{-0.01}$	177^{+46}_{-50}	$0.04^{+0.01}_{-0.01}$	…	…	12.4
25	GW190427_180650	$11.4^{+8.3}_{-2.7}$	$6.4^{+1.8}_{-2.4}$	$7.3^{+0.4}_{-0.4}$	$1.8^{+3.2}_{-0.7}$	$-0.02^{+0.22}_{-0.17}$	983^{+374}_{-412}	$0.2^{+0.06}_{-0.08}$	$17.1^{+6.1}_{-1.4}$	$0.65^{+0.06}_{-0.09}$	9.3
26	GW190503_185404	$42.0^{+10.6}_{-7.9}$	$27.4^{+7.6}_{-8.5}$	$29.0^{+4.5}_{-3.8}$	$1.5^{+1.1}_{-0.5}$	$-0.04^{+0.21}_{-0.29}$	1504^{+575}_{-582}	$0.28^{+0.09}_{-0.1}$	$66.4^{+9.2}_{-7.1}$	$0.66^{+0.09}_{-0.14}$	12.4
27	GW190512_180714	$23.1^{+5.8}_{-5.5}$	$12.4^{+3.5}_{-2.6}$	$14.5^{+1.3}_{-0.9}$	$1.9^{+1.0}_{-0.7}$	$0.03^{+0.13}_{-0.14}$	1522^{+460}_{-568}	$0.29^{+0.07}_{-0.1}$	$34.2^{+4.0}_{-3.3}$	$0.66^{+0.07}_{-0.07}$	12.4
28	GW190513_205428	$35.2^{+9.8}_{-9.1}$	$17.6^{+7.4}_{-4.6}$	$21.2^{+3.2}_{-2.0}$	$2.0^{+1.3}_{-0.9}$	$0.11^{+0.22}_{-0.19}$	2191^{+772}_{-822}	$0.39^{+0.11}_{-0.13}$	$50.9^{+7.4}_{-5.9}$	$0.69^{+0.12}_{-0.13}$	12.5
29	GW190514_065416	$41.1^{+21.7}_{-9.3}$	$28.3^{+9.1}_{-9.5}$	$29.4^{+7.5}_{-5.3}$	$1.4^{+1.5}_{-0.4}$	$-0.16^{+0.28}_{-0.32}$	3935^{+2513}_{-1943}	$0.64^{+0.32}_{-0.28}$	$67.0^{+19.5}_{-11.6}$	$0.63^{+0.11}_{-0.15}$	8.4
30	GW190517_055101	$39.0^{+10.0}_{-7.9}$	$24.2^{+6.1}_{-5.4}$	$26.6^{+2.8}_{-3.4}$	$1.6^{+0.9}_{-0.5}$	$0.51^{+0.16}_{-0.18}$	1785^{+1326}_{-787}	$0.33^{+0.2}_{-0.13}$	$59.7^{+7.4}_{-7.7}$	$0.87^{+0.04}_{-0.05}$	11.6
31	GW190519_153544	$63.1^{+10.1}_{-10.6}$	$40.3^{+11.1}_{-13.5}$	$43.3^{+6.2}_{-7.6}$	$1.6^{+1.0}_{-0.4}$	$0.34^{+0.2}_{-0.25}$	2721^{+1823}_{-1028}	$0.47^{+0.25}_{-0.16}$	$97.6^{+11.6}_{-12.5}$	$0.79^{+0.08}_{-0.11}$	13.9
32	GW190521_030229	$99.8^{+16.9}_{-19.2}$	$58.6^{+17.1}_{-15.8}$	$65.4^{+9.8}_{-8.7}$	$1.7^{+0.8}_{-0.6}$	$-0.15^{+0.41}_{-0.4}$	3147^{+2333}_{-1516}	$0.53^{+0.31}_{-0.23}$	$151.3^{+20.2}_{-15.2}$	$0.61^{+0.15}_{-0.22}$	15.5
33	GW190521_074359	$42.7^{+4.6}_{-4.1}$	$34.4^{+4.9}_{-5.9}$	$33.2^{+2.6}_{-2.7}$	$1.2^{+0.4}_{-0.2}$	$0.09^{+0.1}_{-0.1}$	1007^{+453}_{-386}	$0.2^{+0.08}_{-0.07}$	$73.2^{+5.2}_{-5.0}$	$0.71^{+0.04}_{-0.04}$	24.5
34	GW190527_092055	$37.1^{+18.0}_{-8.9}$	$21.6^{+9.5}_{-8.9}$	$24.0^{+6.6}_{-4.0}$	$1.7^{+2.3}_{-0.6}$	$0.09^{+0.25}_{-0.27}$	2317^{+1780}_{-1107}	$0.41^{+0.25}_{-0.18}$	$56.6^{+16.7}_{-8.6}$	$0.7^{+0.12}_{-0.18}$	8.9
35	GW190602_175927	$70.8^{+17.6}_{-14.3}$	$43.7^{+15.5}_{-18.0}$	$47.3^{+9.2}_{-9.2}$	$1.6^{+1.6}_{-0.5}$	$0.1^{+0.24}_{-0.28}$	2847^{+1795}_{-1203}	$0.49^{+0.24}_{-0.18}$	$109.0^{+16.9}_{-14.4}$	$0.71^{+0.11}_{-0.16}$	12.4
36	GW190620_030421	$61.8^{+22.8}_{-15.0}$	$29.7^{+14.9}_{-11.7}$	$36.6^{+7.8}_{-6.5}$	$2.1^{+2.3}_{-0.9}$	$0.3^{+0.22}_{-0.33}$	2821^{+1419}_{-1309}	$0.49^{+0.2}_{-0.2}$	$88.3^{+17.7}_{-12.2}$	$0.8^{+0.08}_{-0.16}$	12.3
37	GW190630_185205	$34.4^{+7.1}_{-5.1}$	$22.9^{+5.4}_{-4.7}$	$24.3^{+2.3}_{-1.8}$	$1.5^{+0.7}_{-0.4}$	$0.1^{+0.14}_{-0.13}$	1108^{+475}_{-465}	$0.22^{+0.08}_{-0.08}$	$55.0^{+4.8}_{-4.0}$	$0.7^{+0.06}_{-0.07}$	15.6
38	GW190701_203306	$54.8^{+11.3}_{-7.6}$	$41.6^{+8.3}_{-12.1}$	$41.0^{+5.3}_{-4.9}$	$1.3^{+0.8}_{-0.3}$	$-0.09^{+0.22}_{-0.29}$	2027^{+750}_{-738}	$0.37^{+0.11}_{-0.12}$	$91.8^{+10.7}_{-8.7}$	$0.66^{+0.09}_{-0.12}$	12.1
39	GW190706_222641	$69.6^{+14.4}_{-15.1}$	$36.8^{+14.4}_{-13.3}$	$42.7^{+9.2}_{-7.1}$	$1.9^{+1.5}_{-0.7}$	$0.24^{+0.26}_{-0.33}$	4264^{+2278}_{-1791}	$0.68^{+0.29}_{-0.25}$	$100.8^{+16.4}_{-12.3}$	$0.78^{+0.1}_{-0.18}$	13.0
40	GW190707_093326	$11.6^{+2.7}_{-1.6}$	$8.2^{+1.3}_{-1.5}$	$8.5^{+0.4}_{-0.4}$	$1.4^{+0.7}_{-0.3}$	$-0.06^{+0.1}_{-0.08}$	836^{+332}_{-289}	$0.17^{+0.06}_{-0.05}$	$19.1^{+1.3}_{-1.1}$	$0.66^{+0.04}_{-0.03}$	13.1
41	GW190708_232457	$18.0^{+4.7}_{-2.7}$	$12.5^{+2.1}_{-2.5}$	$12.9^{+0.7}_{-0.5}$	$1.4^{+0.8}_{-0.4}$	$0.02^{+0.1}_{-0.07}$	987^{+267}_{-332}	$0.2^{+0.05}_{-0.06}$	$29.2^{+2.5}_{-1.6}$	$0.68^{+0.04}_{-0.04}$	13.0
42	GW190719_215514	$38.1^{+40.0}_{-11.9}$	$19.9^{+11.7}_{-8.6}$	$23.1^{+14.0}_{-4.3}$	$1.9^{+3.7}_{-0.8}$	$0.21^{+0.35}_{-0.29}$	3673^{+3066}_{-2024}	$0.61^{+0.39}_{-0.3}$	$55.6^{+41.7}_{-11.3}$	$0.74^{+0.14}_{-0.21}$	8.2
43	GW190720_000836	$13.5^{+4.9}_{-3.1}$	$7.3^{+2.0}_{-1.8}$	$8.6^{+0.4}_{-0.5}$	$1.8^{+1.4}_{-0.7}$	$0.19^{+0.13}_{-0.1}$	1073^{+402}_{-328}	$0.21^{+0.07}_{-0.06}$	$20.0^{+3.3}_{-1.7}$	$0.73^{+0.05}_{-0.04}$	10.8
44	GW190725_174728	$11.5^{+5.8}_{-2.6}$	$6.4^{+1.9}_{-1.9}$	$7.4^{+0.5}_{-0.4}$	$1.8^{+2.0}_{-0.7}$	$-0.05^{+0.25}_{-0.14}$	1064^{+442}_{-397}	$0.21^{+0.08}_{-0.07}$	$17.3^{+4.0}_{-1.5}$	$0.65^{+0.08}_{-0.06}$	10.0
45	GW190727_060333	$38.2^{+8.0}_{-5.5}$	$29.5^{+6.2}_{-8.1}$	$28.8^{+4.3}_{-3.4}$	$1.3^{+0.8}_{-0.2}$	$0.05^{+0.23}_{-0.24}$	3057^{+1162}_{-1176}	$0.52^{+0.16}_{-0.17}$	$64.1^{+8.7}_{-6.4}$	$0.71^{+0.09}_{-0.1}$	11.7
46	GW190728_064510	$13.5^{+6.1}_{-3.1}$	$7.6^{+2.0}_{-2.1}$	$8.7^{+0.5}_{-0.3}$	$1.8^{+1.8}_{-0.7}$	$0.15^{+0.18}_{-0.09}$	843^{+247}_{-335}	$0.17^{+0.04}_{-0.06}$	$20.2^{+4.2}_{-1.6}$	$0.71^{+0.04}_{-0.04}$	13.8
47	GW190731_140936	$40.9^{+11.3}_{-8.4}$	$29.3^{+9.1}_{-10.2}$	$29.6^{+6.5}_{-5.6}$	$1.4^{+1.1}_{-0.3}$	$0.01^{+0.25}_{-0.27}$	3323^{+2345}_{-1638}	$0.56^{+0.31}_{-0.24}$	$66.9^{+13.4}_{-11.1}$	$0.69^{+0.1}_{-0.13}$	8.5
48	GW190803_022701	$37.2^{+10.3}_{-6.8}$	$27.5^{+7.1}_{-7.7}$	$27.5^{+5.3}_{-3.9}$	$1.3^{+0.9}_{-0.3}$	$-0.0^{+0.24}_{-0.26}$	3407^{+1719}_{-1551}	$0.57^{+0.23}_{-0.23}$	$61.6^{+11.4}_{-8.0}$	$0.69^{+0.09}_{-0.11}$	8.8
49	GW190805_105432	$14.0^{+4.5}_{-3.4}$	$7.5^{+2.1}_{-1.7}$	$8.8^{+0.7}_{-0.6}$	$1.9^{+1.2}_{-0.7}$	$-0.1^{+0.18}_{-0.14}$	1446^{+597}_{-558}	$0.27^{+0.1}_{-0.1}$	$20.7^{+3.3}_{-2.1}$	$0.62^{+0.05}_{-0.05}$	8.9
50	GW190814_211039	$23.3^{+1.4}_{-2.0}$	$2.6^{+0.2}_{-0.1}$	$6.1^{+0.1}_{-0.1}$	$9.0^{+1.0}_{-1.2}$	$-0.01^{+0.07}_{-0.12}$	234^{+39}_{-40}	$0.05^{+0.01}_{-0.01}$	$25.6^{+1.4}_{-1.8}$	$0.28^{+0.03}_{-0.04}$	25.3
51	GW190828_063405	$31.7^{+4.7}_{-3.7}$	$26.3^{+4.3}_{-4.1}$	$24.9^{+3.1}_{-1.9}$	$1.2^{+0.3}_{-0.2}$	$0.18^{+0.13}_{-0.14}$	2179^{+645}_{-903}	$0.39^{+0.1}_{-0.14}$	$54.7^{+6.6}_{-4.1}$	$0.75^{+0.06}_{-0.05}$	16.1
52	GW190828_065509	$24.3^{+5.6}_{-7.1}$	$10.4^{+3.5}_{-2.0}$	$13.5^{+1.2}_{-0.9}$	$2.3^{+1.1}_{-1.1}$	$0.05^{+0.15}_{-0.14}$	1474^{+603}_{-570}	$0.28^{+0.1}_{-0.1}$	$33.5^{+4.3}_{-4.6}$	$0.64^{+0.08}_{-0.07}$	11.4
53	GW190910_112807	$43.8^{+7.2}_{-6.8}$	$32.2^{+6.6}_{-6.5}$	$32.4^{+3.9}_{-3.6}$	$1.4^{+0.5}_{-0.3}$	$-0.03^{+0.16}_{-0.2}$	1699^{+1008}_{-726}	$0.32^{+0.15}_{-0.12}$	$72.5^{+8.0}_{-7.5}$	$0.67^{+0.07}_{-0.09}$	13.7
54	GW190915_235702	$31.8^{+6.2}_{-4.1}$	$24.7^{+4.2}_{-5.0}$	$24.2^{+2.6}_{-2.0}$	$1.3^{+0.6}_{-0.2}$	$-0.03^{+0.17}_{-0.2}$	1801^{+612}_{-677}	$0.33^{+0.09}_{-0.11}$	$54.0^{+5.4}_{-4.2}$	$0.68^{+0.07}_{-0.07}$	13.5
55	GW190916_200658	$43.9^{+18.7}_{-12.3}$	$24.8^{+12.4}_{-11.1}$	$27.9^{+8.6}_{-6.4}$	$1.7^{+2.4}_{-0.6}$	$0.15^{+0.31}_{-0.29}$	4833^{+3600}_{-2366}	$0.76^{+0.43}_{-0.32}$	$66.3^{+17.4}_{-13.9}$	$0.72^{+0.13}_{-0.21}$	7.9
56	GW190924_021846	$8.8^{+4.4}_{-1.9}$	$5.0^{+1.3}_{-1.5}$	$5.7^{+0.2}_{-0.2}$	$1.8^{+2.0}_{-0.7}$	$0.02^{+0.23}_{-0.09}$	598^{+168}_{-184}	$0.12^{+0.03}_{-0.04}$	$13.2^{+3.0}_{-0.9}$	$0.66^{+0.05}_{-0.05}$	12.6
57	GW190925_232845	$20.9^{+6.1}_{-2.9}$	$15.3^{+2.5}_{-3.5}$	$15.5^{+0.9}_{-0.9}$	$1.4^{+0.9}_{-0.3}$	$0.06^{+0.15}_{-0.13}$	928^{+396}_{-306}	$0.19^{+0.07}_{-0.06}$	$34.7^{+3.1}_{-2.2}$	$0.7^{+0.06}_{-0.05}$	9.9
58	GW190926_050336	$40.0^{+20.9}_{-10.9}$	$23.8^{+10.7}_{-9.4}$	$26.2^{+9.3}_{-5.7}$	$1.7^{+1.7}_{-0.6}$	$-0.05^{+0.27}_{-0.33}$	3575^{+3193}_{-1896}	$0.59^{+0.41}_{-0.28}$	$61.2^{+24.2}_{-12.1}$	$0.65^{+0.13}_{-0.18}$	8.8

Table 4
(Continued)

	Event	$m_1/M_\odot$	$m_2/M_\odot$	$\mathcal{M}/M_\odot$	q	$\chi_{\rm eff}$	$D_{\rm L}$/Mpc	z	$M_{\rm f}/M_\odot$	χ_f	S/N
59	GW190929_012149	$66.5^{+16.4}_{-15.7}$	$25.9^{+14.6}_{-9.5}$	$35.1^{+8.5}_{-6.7}$	$2.6^{+2.1}_{-1.2}$	$-0.03^{+0.22}_{-0.25}$	3035^{+2251}_{-1299}	$0.52^{+0.3}_{-0.19}$	$90.2^{+15.1}_{-13.6}$	$0.58^{+0.16}_{-0.2}$	10.3
60	GW190930_133541	$12.7^{+10.6}_{-2.8}$	$7.5^{+1.9}_{-2.9}$	$8.4^{+0.4}_{-0.4}$	$1.7^{+3.4}_{-0.6}$	$0.16^{+0.29}_{-0.14}$	847^{+339}_{-269}	$0.17^{+0.06}_{-0.05}$	$19.3^{+7.8}_{-1.4}$	$0.73^{+0.08}_{-0.06}$	10.2
61	GW191105_143521	$11.0^{+3.6}_{-1.8}$	$7.3^{+1.5}_{-1.7}$	$7.8^{+0.5}_{-0.4}$	$1.5^{+1.1}_{-0.4}$	$-0.0^{+0.14}_{-0.09}$	1196^{+361}_{-437}	$0.23^{+0.06}_{-0.08}$	$17.7^{+2.0}_{-1.2}$	$0.67^{+0.05}_{-0.04}$	10.2
62	GW191109_010717	$64.0^{+14.9}_{-11.7}$	$50.1^{+13.5}_{-14.4}$	$48.4^{+10.8}_{-8.5}$	$1.3^{+0.6}_{-0.2}$	$-0.08^{+0.46}_{-0.5}$	1555^{+1161}_{-670}	$0.29^{+0.18}_{-0.12}$	$107.7^{+22.0}_{-16.9}$	$0.68^{+0.18}_{-0.23}$	16.5
63	GW191126_115259	$12.4^{+5.7}_{-2.4}$	$8.0^{+1.8}_{-2.3}$	$8.6^{+0.8}_{-0.7}$	$1.5^{+1.6}_{-0.5}$	$0.23^{+0.14}_{-0.13}$	1710^{+688}_{-653}	$0.32^{+0.11}_{-0.11}$	$19.6^{+3.7}_{-1.9}$	$0.75^{+0.07}_{-0.05}$	8.7
64	GW191127_050227	$52.2^{+42.7}_{-23.0}$	$19.4^{+15.4}_{-11.0}$	$25.5^{+12.2}_{-7.1}$	$2.6^{+6.8}_{-1.5}$	$0.08^{+0.39}_{-0.37}$	3015^{+3202}_{-1581}	$0.51^{+0.42}_{-0.24}$	$70.6^{+37.1}_{-22.1}$	$0.7^{+0.17}_{-0.32}$	10.0
65	GW191129_134029	$10.9^{+3.9}_{-2.2}$	$6.6^{+1.6}_{-1.5}$	$7.3^{+0.4}_{-0.2}$	$1.7^{+1.2}_{-0.6}$	$0.07^{+0.15}_{-0.08}$	813^{+221}_{-297}	$0.16^{+0.04}_{-0.06}$	$16.8^{+2.4}_{-1.1}$	$0.69^{+0.04}_{-0.04}$	13.2
66	GW191204_110529	$27.8^{+9.6}_{-5.9}$	$19.2^{+5.2}_{-6.1}$	$20.0^{+3.1}_{-3.3}$	$1.4^{+1.3}_{-0.4}$	$0.07^{+0.22}_{-0.22}$	1794^{+1641}_{-953}	$0.33^{+0.24}_{-0.16}$	$45.4^{+6.9}_{-7.5}$	$0.7^{+0.1}_{-0.1}$	9.6
67	GW191204_171526	$12.7^{+3.5}_{-2.4}$	$7.9^{+1.6}_{-1.5}$	$8.7^{+0.3}_{-0.3}$	$1.6^{+0.9}_{-0.5}$	$0.17^{+0.1}_{-0.05}$	582^{+204}_{-187}	$0.12^{+0.04}_{-0.04}$	$19.7^{+2.1}_{-1.2}$	$0.73^{+0.04}_{-0.04}$	17.6
68	GW191215_223052	$24.6^{+6.1}_{-3.7}$	$18.3^{+3.5}_{-4.0}$	$18.3^{+1.9}_{-1.6}$	$1.3^{+0.8}_{-0.3}$	$-0.06^{+0.18}_{-0.21}$	1935^{+881}_{-807}	$0.35^{+0.13}_{-0.13}$	$41.2^{+4.3}_{-3.8}$	$0.68^{+0.07}_{-0.07}$	11.5
69	GW191216_213338	$12.4^{+3.9}_{-2.6}$	$7.4^{+1.8}_{-1.6}$	$8.3^{+0.2}_{-0.2}$	$1.7^{+1.1}_{-0.6}$	$0.11^{+0.13}_{-0.07}$	362^{+98}_{-119}	$0.08^{+0.02}_{-0.02}$	$19.0^{+2.4}_{-1.0}$	$0.7^{+0.04}_{-0.04}$	18.6
70	GW191222_033537	$45.1^{+9.7}_{-7.9}$	$33.9^{+9.1}_{-9.5}$	$33.5^{+6.5}_{-4.9}$	$1.3^{+0.8}_{-0.3}$	$-0.09^{+0.19}_{-0.27}$	3147^{+1705}_{-1513}	$0.53^{+0.23}_{-0.23}$	$75.2^{+13.5}_{-10.0}$	$0.66^{+0.08}_{-0.1}$	12.0
71	**GW191224_043228**	$14.2^{+5.6}_{-3.4}$	$7.9^{+2.3}_{-2.0}$	$9.2^{+0.7}_{-0.6}$	$1.8^{+1.5}_{-0.7}$	$0.08^{+0.16}_{-0.11}$	1804^{+596}_{-576}	$0.33^{+0.09}_{-0.09}$	$21.4^{+3.9}_{-2.1}$	$0.69^{+0.06}_{-0.05}$	9.0
72	GW191230_180458	$49.5^{+12.5}_{-9.3}$	$36.3^{+11.0}_{-11.7}$	$36.2^{+8.3}_{-5.9}$	$1.3^{+0.9}_{-0.3}$	$-0.01^{+0.25}_{-0.28}$	4212^{+2139}_{-1838}	$0.68^{+0.27}_{-0.26}$	$81.3^{+17.2}_{-11.6}$	$0.69^{+0.1}_{-0.11}$	10.4
73	GW200105_162426	$8.7^{+1.5}_{-1.6}$	$1.9^{+0.4}_{-0.2}$	$3.4^{+0.1}_{-0.1}$	$4.5^{+1.4}_{-1.4}$	$-0.01^{+0.12}_{-0.16}$	298^{+93}_{-113}	$0.06^{+0.02}_{-0.02}$	$10.4^{+1.3}_{-1.3}$	$0.45^{+0.06}_{-0.02}$	13.4
74	**GW200106_134123**	$44.0^{+13.9}_{-10.9}$	$27.4^{+10.9}_{-9.9}$	$29.7^{+7.5}_{-6.0}$	$1.6^{+1.4}_{-0.5}$	$0.1^{+0.29}_{-0.31}$	3989^{+3214}_{-1864}	$0.65^{+0.4}_{-0.27}$	$68.4^{+15.3}_{-13.0}$	$0.71^{+0.12}_{-0.17}$	8.6
75	GW200112_155838	$37.6^{+6.4}_{-5.3}$	$27.1^{+5.0}_{-5.3}$	$27.6^{+2.3}_{-2.2}$	$1.4^{+0.6}_{-0.3}$	$0.07^{+0.14}_{-0.14}$	1142^{+474}_{-362}	$0.22^{+0.08}_{-0.06}$	$61.8^{+4.6}_{-4.6}$	$0.7^{+0.06}_{-0.06}$	18.6
76	GW200115_042309	$6.6^{+0.8}_{-1.2}$	$1.3^{+0.2}_{-0.1}$	$2.4^{+0.0}_{-0.1}$	$5.2^{+1.1}_{-1.6}$	$-0.03^{+0.08}_{-0.16}$	393^{+123}_{-93}	$0.08^{+0.02}_{-0.02}$	$7.8^{+0.7}_{-1.0}$	$0.4^{+0.07}_{-0.02}$	10.9
77	GW200128_022011	$40.7^{+11.2}_{-8.0}$	$30.3^{+9.1}_{-8.4}$	$30.1^{+7.1}_{-4.9}$	$1.3^{+0.8}_{-0.3}$	$0.07^{+0.22}_{-0.23}$	3609^{+2097}_{-1885}	$0.6^{+0.27}_{-0.28}$	$67.3^{+15.1}_{-10.3}$	$0.72^{+0.09}_{-0.1}$	10.2
78	GW200129_065458	$40.3^{+6.6}_{-7.8}$	$23.4^{+8.7}_{-4.4}$	$26.7^{+2.5}_{-2.0}$	$1.7^{+0.7}_{-0.7}$	$0.09^{+0.13}_{-0.16}$	911^{+189}_{-327}	$0.18^{+0.03}_{-0.06}$	$61.5^{+4.0}_{-3.3}$	$0.76^{+0.07}_{-0.06}$	27.1
79	**GW200129_114245**	$79.1^{+40.2}_{-37.6}$	$31.5^{+18.6}_{-14.4}$	$41.0^{+15.7}_{-13.1}$	$2.3^{+3.7}_{-1.2}$	$0.13^{+0.4}_{-0.38}$	5294^{+4287}_{-2561}	$0.82^{+0.51}_{-0.34}$	$109.6^{+34.9}_{-42.4}$	$0.73^{+0.16}_{-0.21}$	8.3
80	GW200202_154313	$10.6^{+3.6}_{-1.8}$	$7.0^{+1.4}_{-1.5}$	$7.4^{+0.2}_{-0.2}$	$1.5^{+1.1}_{-0.5}$	$0.04^{+0.14}_{-0.06}$	442^{+130}_{-120}	$0.09^{+0.03}_{-0.02}$	$16.8^{+2.1}_{-0.7}$	$0.68^{+0.03}_{-0.03}$	11.2
81	GW200208_130117	$37.6^{+9.0}_{-6.0}$	$27.2^{+5.9}_{-6.8}$	$27.5^{+3.4}_{-2.9}$	$1.4^{+0.8}_{-0.3}$	$-0.07^{+0.21}_{-0.26}$	2259^{+952}_{-844}	$0.4^{+0.14}_{-0.13}$	$62.2^{+7.1}_{-6.1}$	$0.66^{+0.08}_{-0.11}$	11.0
82	GW200209_085452	$34.8^{+9.3}_{-6.2}$	$25.3^{+7.0}_{-8.0}$	$25.4^{+5.0}_{-3.9}$	$1.4^{+1.0}_{-0.3}$	$-0.08^{+0.24}_{-0.3}$	3573^{+1779}_{-1631}	$0.59^{+0.23}_{-0.24}$	$57.2^{+10.8}_{-7.4}$	$0.67^{+0.09}_{-0.13}$	9.4
83	**GW200210_005122**	$8.9^{+3.5}_{-1.6}$	$5.9^{+1.2}_{-1.5}$	$6.3^{+0.3}_{-0.4}$	$1.5^{+1.3}_{-0.5}$	$0.06^{+0.17}_{-0.09}$	1299^{+490}_{-343}	$0.25^{+0.08}_{-0.06}$	$14.3^{+2.1}_{-1.1}$	$0.69^{+0.06}_{-0.05}$	8.5
84	**GW200214_223307**	$51.6^{+24.4}_{-14.2}$	$30.9^{+15.5}_{-12.0}$	$34.2^{+12.5}_{-7.9}$	$1.6^{+1.8}_{-0.5}$	$0.01^{+0.28}_{-0.28}$	5161^{+4122}_{-2714}	$0.8^{+0.49}_{-0.37}$	$79.6^{+28.8}_{-17.8}$	$0.68^{+0.12}_{-0.17}$	7.9
85	GW200216_220804	$51.7^{+16.5}_{-11.5}$	$31.6^{+12.9}_{-15.2}$	$34.2^{+8.1}_{-8.2}$	$1.6^{+2.3}_{-0.5}$	$0.06^{+0.29}_{-0.31}$	3643^{+2367}_{-1708}	$0.6^{+0.3}_{-0.25}$	$79.5^{+15.7}_{-12.4}$	$0.7^{+0.12}_{-0.19}$	8.7
86	GW200219_094415	$37.7^{+10.1}_{-7.2}$	$27.6^{+7.6}_{-8.3}$	$27.7^{+5.3}_{-4.3}$	$1.3^{+0.9}_{-0.3}$	$-0.11^{+0.23}_{-0.28}$	3214^{+1919}_{-1396}	$0.54^{+0.25}_{-0.21}$	$62.5^{+11.3}_{-8.8}$	$0.65^{+0.09}_{-0.12}$	10.5
87	GW200224_222234	$40.1^{+6.2}_{-4.6}$	$32.2^{+4.9}_{-6.6}$	$30.9^{+3.1}_{-2.4}$	$1.2^{+0.5}_{-0.2}$	$0.1^{+0.14}_{-0.15}$	1683^{+474}_{-624}	$0.31^{+0.07}_{-0.1}$	$68.3^{+6.2}_{-4.4}$	$0.73^{+0.06}_{-0.07}$	19.1
88	GW200225_060421	$19.1^{+4.0}_{-2.6}$	$14.7^{+2.5}_{-2.9}$	$14.5^{+1.4}_{-1.1}$	$1.3^{+0.6}_{-0.3}$	$-0.12^{+0.14}_{-0.15}$	1103^{+598}_{-560}	$0.22^{+0.1}_{-0.1}$	$32.4^{+3.0}_{-2.7}$	$0.66^{+0.06}_{-0.06}$	12.9
89	GW200302_015811	$38.5^{+8.2}_{-8.4}$	$21.5^{+7.2}_{-6.5}$	$24.5^{+3.9}_{-3.5}$	$1.8^{+1.1}_{-0.7}$	$0.03^{+0.22}_{-0.25}$	1582^{+996}_{-723}	$0.3^{+0.15}_{-0.12}$	$57.5^{+7.7}_{-7.0}$	$0.68^{+0.11}_{-0.14}$	11.2
90	**GW200305_084739**	$33.8^{+12.1}_{-7.7}$	$23.2^{+7.7}_{-9.4}$	$24.0^{+5.9}_{-5.4}$	$1.4^{+1.5}_{-0.4}$	$-0.02^{+0.29}_{-0.32}$	4422^{+2903}_{-2113}	$0.7^{+0.36}_{-0.29}$	$54.5^{+13.1}_{-10.2}$	$0.68^{+0.12}_{-0.15}$	8.1
91	GW200306_093714	$27.5^{+13.5}_{-6.9}$	$15.4^{+5.4}_{-6.1}$	$17.7^{+2.9}_{-3.1}$	$1.8^{+2.4}_{-0.7}$	$0.32^{+0.24}_{-0.41}$	2249^{+1478}_{-1056}	$0.4^{+0.21}_{-0.17}$	$41.3^{+9.4}_{-6.5}$	$0.79^{+0.09}_{-0.22}$	8.1
92	GW200311_115853	$34.6^{+6.1}_{-3.9}$	$26.5^{+4.3}_{-5.5}$	$26.1^{+2.2}_{-1.7}$	$1.3^{+0.6}_{-0.3}$	$-0.04^{+0.14}_{-0.17}$	1187^{+245}_{-370}	$0.23^{+0.04}_{-0.07}$	$58.3^{+4.4}_{-3.3}$	$0.67^{+0.07}_{-0.07}$	17.7
93	GW200316_215756	$13.9^{+10.2}_{-3.7}$	$7.3^{+2.2}_{-2.6}$	$8.7^{+0.5}_{-0.5}$	$1.9^{+3.2}_{-0.8}$	$0.14^{+0.27}_{-0.12}$	1206^{+452}_{-412}	$0.23^{+0.08}_{-0.07}$	$20.4^{+7.8}_{-2.1}$	$0.71^{+0.07}_{-0.05}$	10.6
94	**GW200318_191337**	$49.1^{+16.4}_{-12.0}$	$31.6^{+12.0}_{-11.6}$	$33.5^{+8.8}_{-6.4}$	$1.5^{+1.4}_{-0.5}$	$0.08^{+0.28}_{-0.31}$	5513^{+3372}_{-2617}	$0.84^{+0.4}_{-0.35}$	$76.9^{+18.8}_{-13.7}$	$0.71^{+0.11}_{-0.17}$	8.4

Note. The various columns report the median and 90% credible intervals for the source-frame component masses m_1 and m_2, chirp mass $\mathcal{M}$, mass ratio q, effective spin $\chi_{\rm eff}$, luminosity distance $D_{\rm L}$, redshift z, and remnant mass and spin M_f and χ_f, respectively. The S/N is computed from the maximum likelihood for BBH events and the maximum likelihood analytically marginalized over the phase for NSBH or BNS events. The quoted results for BBH, BNS, and NSBH events are computed using IMRPhenomXPHM, IMRPhenomD_NRTidal, and IMRPhenomNSBH waveform models, respectively.

component masses between 2 and $100M_\odot$. We make available the data products needed to perform more detailed follow-up analyses (Nitz & Kumar 2021); astrophysically motivated models may provide further insights (Stevenson et al. 2019; Fragione & Banerjee 2021).

3.3.1. Parametric Models

The observed mass distribution corrected for first-order selection effects (as shown in Figure 5) clearly shows a peak in the primary mass between 30 and 40 $M_\odot$; this peak was previously reported in Abbott et al. (2021h). This observation motivates a parametric model where the primary mass is modeled with a power-law component along with added Gaussian components to account for peaks in the mass distribution. The power-law component of the primary mass is modeled as $p(m_1) \propto m_1^{\alpha}$. A peak in the observed distribution can be modeled with a Gaussian distribution following Abbott et al. (2021c, 2021h):

$$p(m_1) \propto (1 - \lambda)\mathcal{C}_{pl} m_1^{-\alpha} + \lambda \mathcal{N}(m_1; \mu^M, \sigma^M), \quad (1)$$

where λ represents the fraction of events in the Gaussian component, $\mathcal{C}_{pl}$ is the normalization for power-law component, $\mathcal{N}(x; \mu^M, \sigma^M)$ is the probability density function for a normal distribution for mean μ^M and standard deviation σ^M. An additional smoothing function is applied at the low end of the mass distribution in Equation (1), i.e., $m_{\rm min} <= m_1 < m_{\rm min} + \delta_M$, where δ_M is the length of the smoothing window. The other population parameters for this model are the minimum $m_{\rm min}$ and maximum $m_{\rm max}$ masses. The conditional probability distribution

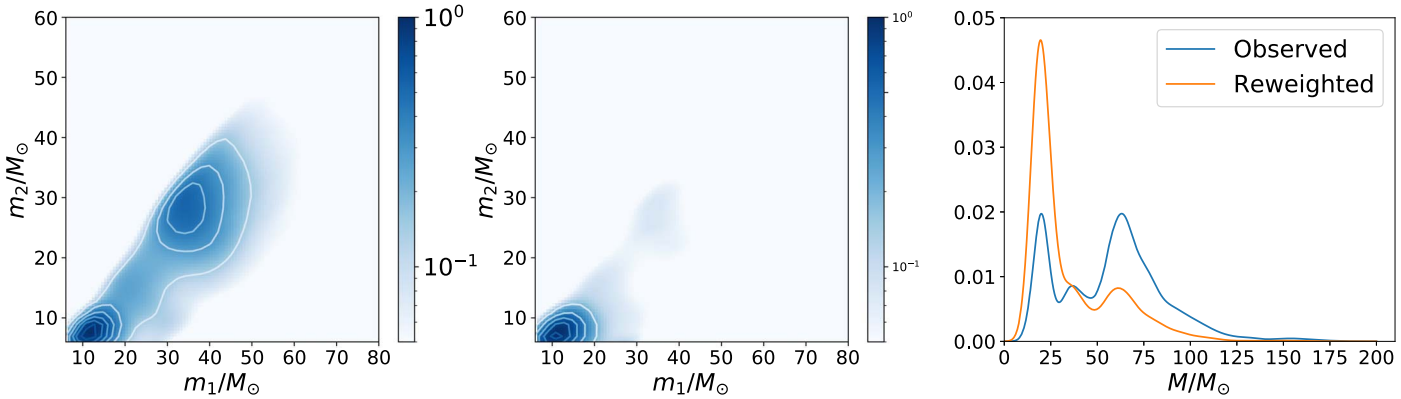

Figure 5. Distribution of the source-frame component masses of the BBH population obtained from combining posteriors from all the confident BBH events in the 4-OGC analysis. We show the observed component mass distribution (left), component mass distribution corrected for the basic selection effect (middle), and the one-dimensional marginals of the total mass distributions for both the observed population as well as corrected for selection effects (right). To correct for selection effects, we assume a constant detection threshold and correct the distribution for signal loudness varying with component masses.

for the secondary mass m_2 is parameterized in terms of mass ratio $q_{pl} = m_2/m_1$, such that $p(q_{pl}|m_1) \propto q_{pl}^{\beta}$ with the same smoothing function at the lower end of m_2. We distinguish this definition of mass ratio q_{pl} with a subscript "pl" (power law) from the other definition $q = m_1/m_2$ used elsewhere in the paper. Any additional peak in the primary mass distribution can be added as an additional Gaussian component in Equation (1).

The redshift evolution of the BBH merger rate in local comoving time and space coordinates is also given as a power law (Fishbach et al. 2018) $R(z) = R_0(1+z)^{\kappa}$, where R_0 defines the local merger rate density at $z = 0$ and κ represents the power-law index.

3.3.2. Selection Effects

A search's sensitivity to BBH mergers depends on various factors, such as intrinsic source parameters (such as component masses and spins), extrinsic parameters (such as orientation and sky location of the binary), and the detector sensitivity, and behavior of the search to non-Gaussian transient noise. To infer the intrinsic population distribution, one needs to calculate the detection efficiency of the search, i.e., the fraction of the events that can be detected with a population described by the parameters $\Theta^{\rm pop}$. To estimate the detection efficiency, we add a known fiducial population to the data across the observing time of the detector network and use our search to identify them. We use an up-to-date waveform model, which includes higher modes and precession, IMRPhenomXPHM (LALSuite 2020; Pratten et al. 2021), to simulate the fiducial population. The reference population follows a power-law mass model on m_1 and mass ratio q_{pl}, where $p(m_1) \propto m_1^{-\alpha}$ and $p(q_{pl}|m_1) \propto (q_{pl})^{\beta}$ with $\alpha = 2.35$ and $\beta = 0$. We use an isotropic spin distribution and the redshift evolution model $p\left(z\right) \propto \frac{1}{1+z}\frac{dV_c}{dz}(1+z)^{\kappa}$ with $\kappa = 0$. The selection function is estimated using a Monte Carlo integral using the sources identified by the search as described in Tiwari (2018), Mandel et al. (2019), and Farr (2019):

$$\xi(\Theta^{\rm pop}) = \frac{1}{N_{\rm inj}} \sum_{k=1}^{N_{\rm inj}^{\rm found}} \frac{\pi(\theta_k|\Theta^{\rm pop})}{p_{\rm draw}(\theta_k)}, \tag{2}$$

where $N_{\rm inj}$ is the total number of simulated sources drawn from the fiducial population, $N_{\rm inj}^{\rm found}$ is the number of sources found by the search, and $p_{\rm draw}(\theta_k)$ is the probability to draw a source from the reference population with parameter θ_k, while $\pi(\theta_k|\Theta^{\rm pop})$ represents the conditional probability distribution of the parameter θ_k given the population hyper- parameter $\Theta^{\rm pop}$.

3.3.3. Parameter Estimation for Population Parameters

Given the total number of detections $N_{\rm det}$, data d, and the population model described by hyper-parameter $\Theta^{\rm pop}$, the population likelihood function can be described by inhomogeneous Poisson processes given as (Loredo 2004; Mandel et al. 2019; Thrane & Talbot 2020; Abbott et al. 2021h)

$$\begin{aligned}&\mathcal{L}(\{d\}, N_{\rm det}|\Theta^{\rm pop}, N_{\rm exp})\\ &\propto N^{N_{\rm det}} e^{-N_{\rm exp}} \prod_{i=1}^{N_{\rm det}} \int \mathcal{L}(d_i|\theta)\pi(\theta|\Theta^{\rm pop})d\theta,\end{aligned} \tag{3}$$

where θ is the set of individual source parameters. $\mathcal{L}(d_i|\theta)$ is the likelihood function of the ith observation. $N_{\rm exp}$ is the expected number of detections over the full observation period. The total number of mergers N during the same period is given by $N = N_{\rm exp}/\xi(\Theta^{\rm pop})$.

We select candidates that pass the following selection criteria: IFAR >100 yr or $P_{\rm astro} > 0.9$. A total of 69 BBH events in the 4-OGC catalog satisfy this criteria. We further identify GW190814_211039 as an outlier from the observed population and exclude it from further analysis due to its very high mass ratio and very low secondary component mass. We use flat priors on all population hyper-parameters except for a log uniform prior on rate parameter R_0. We allow the maximum primary mass to vary up to $150M_\odot$. We use three models for primary mass: (i) pure power-law component, (ii) power law + peak , and (iii) power law + two peaks. We use a uniform prior for the location of the first peak between 20 and $45M_\odot$. For the additional peak in the power law + peak model, we use a uniform prior between 45 and $80M_\odot$.

Figure 6 shows the estimated differential merger rate as a function of the primary mass. The power law + peak model shows a clear peak between 30 and $40M_\odot$. The model with two peaks is consistent and does not indicate the presence of a second peak. The results also broadly agree with the GWTC-3 analysis (Abbott et al. 2021h). The small differences can be attributed to the selected observations, differences in the selection function of both searches, and the explored prior ranges. For example, we allow the maximum mass parameter $m_{\rm max}$ to vary up to 150 $M_\odot$ compared to 100 $M_\odot$ in the GWTC-

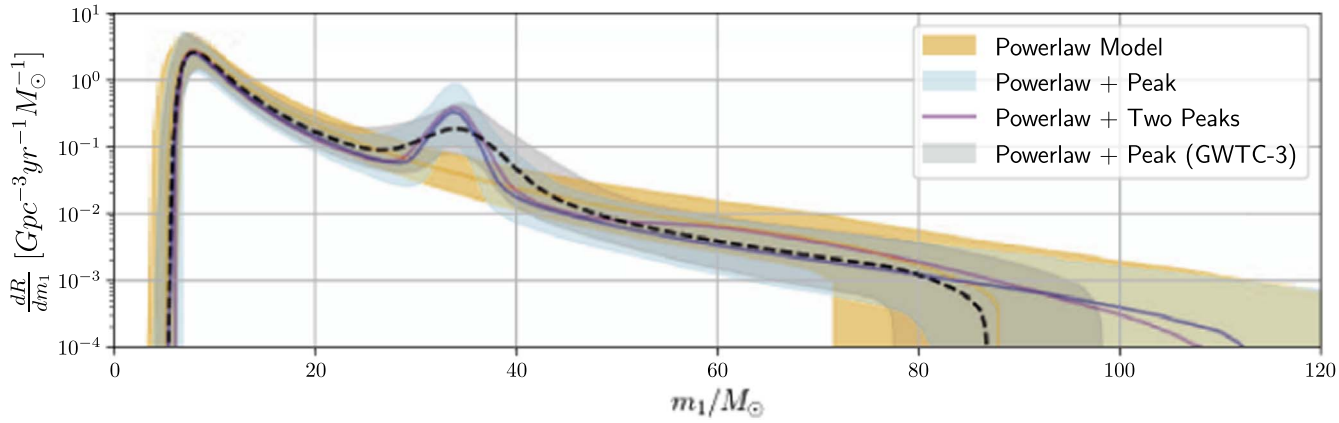

Figure 6. Differential merger rate as a function of source-frame primary mass for the parametric mass models considered in the study: power law (orange), power law + peak (blue), and power law + two peaks (purple). We marginalize over all other population parameters in each model. Solid lines show the median value for the analysis done with 4-OGC events. Shaded regions show the 90% credible intervals; the power law + two peaks model is omitted to improve visual clarity. For comparison, the power law + peak result from GWTC-3 (Abbott et al. 2021h) is shown with a black dashed line and gray shaded region. The maximum likelihood value of λ (representing the fraction of events in the Gaussian component) for the power law + peak model is 0.044. Similarly, the maximum likelihood values of λ_1 and λ_2 for the power law+two peak model are 0.062 and 0.003, respectively.

3 analysis (Abbott et al. 2021h). This explains the differences in the differential merger rate plot at high masses ($>100\,M_\odot$). For all three population models we consider in this study, we calculate the Bayesian evidence ($\mathcal{Z}$) defined as

$$\mathcal{Z} = \int \mathcal{L}(d|\Theta, M)\pi(\Theta|M), \tag{4}$$

where $\mathcal{L}(d|\Theta, M)$ is the likelihood function for the data d given a model M with parameters Θ. $\pi(\Theta|M)$ is the prior function for parameter Θ for the given model. A model with a larger value of $\mathcal{Z}$ is statistically favored (Kass & Raftery 1995; Jeffreys 1998). The ratio of the Bayesian evidence $\mathcal{Z}_1/\mathcal{Z}_2$ for two models is called the Bayes factor $\mathcal{B}_{12}$. The $\log_{10}(\mathcal{B}_{12})$ is $\sim$1 and 4 in favor of the power law + peak model with respect to the power law + two peak and power-law models, respectively. The Bayesian information criteria (Kass & Raftery 1995) give a consistent model ranking.

The fraction of events in the primary mass Gaussian component of the power law + peak model is represented by the parameter λ in Equation (1). We find $\lambda = 0.046^{+0.071}_{-0.032}$ at the 90% credible level. For the power law + two peak model, there are two Gaussian components in the primary mass function, and the fraction of events in each component is represented by parameters λ_1 and λ_2, where $\lambda_1 = 0.060^{+0.089}_{-0.039}$ and $\lambda_2 < 0.011$ at 90% credible levels. The λ_2 parameter is peaked near zero so we report the upper bound.

Figure 7 shows the redshift evolution of the BBH merger rate for the power law + peak model. Since the majority of mergers are found near redshift $z \sim 0.2$ as expected, the merger rate is best constrained at this redshift. Table 5 shows the merger rates estimated for each model at redshifts $z = 0$ and at $z = 0.2$.

3.4. Neutron Star Binaries and Neutron Star–Black Hole Binaries

GW170817_124104 (Abbott et al. 2017a) and GW190425_081805 (Abbott et al. 2020a) remain the only confidently observed mergers with BNS-compatible masses. GW170817_124104 is observed in both the LIGO-Hanford and LIGO-Livingston data with a joint S/N $\sim$33. This remains the only BNS observation with unambiguous electromagnetic counterparts (Abbott et al. 2017a, 2017b). In addition to the γ-ray burst (GRB 170817A; Abbott et al. 2017d; Goldstein et al. 2017; Savchenko et al. 2017), the successful electromagnetic follow-up campaign that identified the associated electromagnetic transient near the galaxy NGC 4993 (Abbott et al. 2017b) supports the interpretation of this event as a neutron star merger. GW190425_081805 is observed only in

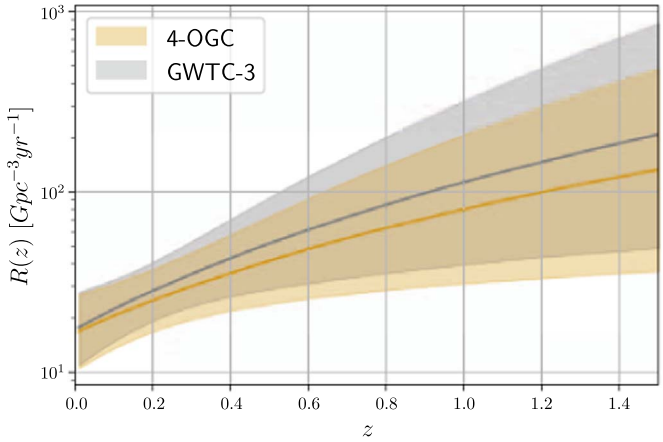

Figure 7. The evolution of the merger rate with redshift is shown for the power law + peak model along with a comparison to the corresponding GWTC-3 result (Abbott et al. 2021h). The merger rate $R(z)$ is constrained best at around redshift $z \sim 0.2$.

Table 5
BBH Merger Rates (90% Credible Interval) for Various Parametric Models at Redshift $z = 0$ and 0.2 Are Shown

Model	Rate $z = 0$	[Gpc^{-3}yr^{-1}] $z = 0.2$
Power-law	$18.47^{+10.92}_{-7.00}$	$30.50^{+15.05}_{-9.56}$
Power law + Peak	$16.53^{+10.36}_{-6.19}$	$24.98^{+12.57}_{-8.06}$
Power law + Two peaks	$17.30^{+10.13}_{-6.65}$	$24.36^{+11.89}_{-7.84}$

Note. We use the parameterization for evolution of merger rates as redshift to be $R(z) = R_0(1+z)^\kappa$. The numbers are quoted for $z = 0.2$ along with $z = 0$ as the constraints on $R(z)$ are stronger at $z = 0.2$.

the LIGO-Livingston data with S/N ∼11.9. However, the long duration of the signal increases the power of signal consistency tests (Usman et al. 2016); given the distinct separation from the measured background distribution, we consider this a firm detection. Its masses $1.7^{+0.1}_{-0.1}\,M_\odot$ and $1.6^{+0.1}_{-0.1}\,M_\odot$ (assuming spin magnitude <0.05) are consistent with interpreting both components as neutron stars. The primary mass is less than the heaviest observed neutron star $\sim 2.2 M_\odot$ (Cromartie et al. 2020); however, galactic BNS observations typically have lower mass (Ozel & Freire 2016). If light black holes in these masses are produced in abundance and form binaries, then we cannot necessarily rule out this explanation from gravitational-wave observation alone.

We observe two events, GW200105_162426 and GW200115_042309, with masses consistent with an NSBH system. GW200105_162426 is observed only in the LIGO-Livingston data with an S/N ∼13.3, whereas GW200115_042309 is observed in both the Livingston and Hanford data with IFAR > 100 yr. We are unable to constrain the tidal deformability of the secondary component, which is consistent with previous results (Abbott et al. 2021d; Zhu et al. 2021).

3.4.1. Merger Rate

For neutron star binaries, we use a simplified approach to merger-rate estimation. We assume that the mergers are Poisson distributed and use a Jeffrey's prior for the rate parameter. We make the simplifying assumption that the observed sources are representative of the mass distribution and do not attempt to fit a mass distribution to the two BNS and two NSBH observations. The observed volume-time for each source class is estimated by simulating the recovery of sources with the same observed source-frame masses and observed low effective spins.

We find that if we consider both GW170817 and GW190425 to be representative members of a common BNS population, we infer the merger rate to be 200^{+309}_{-148} Gpc^{-3} yr^{-1} using 90% credible intervals. However, given the unexpectedly large mass of GW190425, it is useful to consider the limits from GW170817 alone under the assumption that these sources either arise from different mechanisms or GW190425 is not a BNS merger. In this scenario, we find that the BNS merger rate is instead 139^{+319}_{-118} Gpc^{-3} yr^{-1}. Assuming both GW200105 and GW200115 are NSBH mergers, we estimate the merger rate to be 19^{+30}_{-14} Gpc^{-3} yr^{-1}. The merger-rate estimation is dominated by large uncertainties due to the few observed events and the choice of mass distribution. Alternate choices for the assumed mass distribution can lead to different results; a larger population of observed sources is required to disentangle current rate estimates from assumed mass distributions.

4. Data Release

The compilation of supplementary materials is available at https://github.com/gwastro/4-ogc (Nitz & Kumar 2021). To aid in follow-up analyses, the data release contains both the gravitational wave events included in this paper and also the detailed set of subthreshold BNS, NSBH, and BBH candidates. Auxiliary information, such as the parameters of an associated waveform template, ranking statistics, FAR, estimated $\mathcal{P}_{\rm astro}$, results of signal consistency tests, etc., are included where possible. The data release also contains the posterior samples from our parameter estimate for each significant candidate. The configuration files needed to reproduce both the overall search and the individual source parameter estimates are provided. We also provide the data products needed to reproduce the BBH population inference with alternate models; this includes the sensitivity of our search to a reference population. Finally, we make available the posterior samples of the parametric population models used in this study.

5. Conclusions

4-OGC is a comprehensive catalog of gravitational-wave observations from BNS, NSBH, and BBH mergers covering the 2015–2020 time period. The 94 mergers included in the 4-OGC catalog represent the largest collection to date. These include 90 BBHs, 2 BNS, and 2 NSBH mergers. Seven new BBHs during O3b have been reported here that pass our significance threshold. We estimate the merger rate of BNS, NSBH, and BBH sources at $z = 0$ to be 200^{+309}_{-148}, 19^{+30}_{-14}, and 16^{+10}_{-6} yr^{-1}, respectively. The release of our catalog can help enable deeper investigations of gravitational-wave candidates, for instance, to look for deviations from general relativity, study formation channels of compact binary mergers, and correlate results with other archival observations. It is expected that future catalogs may contain hundreds of sources after the ongoing upgrades are completed. The next observing run is scheduled to begin operation at the end of 2022 (Abbott et al. 2020b). The importance of gravitational-wave catalogs will only grow as gravitational-wave astronomy matures, and focus is able to shift to understanding increasingly detailed population features.

We are grateful to the computing team from AEI Hannover for their significant technical support. This research has made use of data from the Gravitational Wave Open Science Center (https://www.gw-openscience.org), a service of LIGO Laboratory, the LIGO Scientific Collaboration and the Virgo Collaboration. LIGO is funded by the U.S. National Science Foundation. Virgo is funded by the French Centre National de Recherche Scientifique (CNRS), the Italian Istituto Nazionale della Fisica Nucleare (INFN) and the Dutch Nikhef, with contributions by Polish and Hungarian institutes.

ORCID iDs

Alexander H. Nitz https://orcid.org/0000-0002-1850-4587
Sumit Kumar https://orcid.org/0000-0002-6404-0517
Yi-Fan Wang (王一帆) https://orcid.org/0000-0002-2928-2916
Shilpa Kastha https://orcid.org/0000-0003-0966-1748
Shichao Wu (吴仕超) https://orcid.org/0000-0002-9188-5435
Marlin Schäfer https://orcid.org/0000-0002-6990-0627
Rahul Dhurkunde https://orcid.org/0000-0002-5077-8916
Collin D. Capano https://orcid.org/0000-0002-0355-5998

References

Aasi, J., Abadie, J., Abbott, B.P., et al. 2013, NaPho, 7, 613
Aasi, J., Abadie, J., Abbott, B.P., et al. 2015, CQGra, 32, 074001
Abadie, J., Abbott, B.P., Abbott, R., et al. 2012, PhRvD, D85, 082002
Abbott, B., Abbott, R., Adhikari, R., et al. 2009, PhRvD, 80, 047101
Abbott, B., Abbot, R., Abbott, T.D., et al. 2017a, PhRvL, 119, 161101
Abbott, B., Abbott, R., Abbott, T.D., et al. 2020a, ApJL, 892, L3
Abbott, B. P., Abbott, R., Abbott, T.D., et al. 2017b, ApJL, 848, L12
Abbott, B. P., Abbott, R., Abbott, T.D., et al. 2017c, ApJL, 851, L35

Abbott, B. P., Abbott, R., Abbott, T. D., et al. 2017d, ApJL, 848, L13
Abbott, B. P., Abbott, R., Abbott, T. D., et al. 2018, CQGra, 35, 065010
Abbott, B. P., Abbott, R., Abbott, T.D., et al. 2019a, PhRvX, 9, 031040
Abbott, B. P., Abbott, R., Abbott, T.D., et al. 2019b, ApJL, 882, L24
Abbott, B. P., Abbott, R., Abbott, T.D., et al. 2020b, LRR, 23, 3
Abbott, R., Abbott, T.D., Abraham, S., et al. 2021a, PhRvX, 11, 021053
Abbott, B. P., Abbott, T.D., Abraham, S., et al. 2020c, PhRvL, 125, 101102
Abbott, R., Abbott, T.D., Abraham, S., et al. 2020d, ApJL, 900, L13
Abbott, R., Abbott, T.D., Abraham, S., et al. 2020e, ApJL, 896, L44
Abbott, R., Abbott, T.D., Abraham, S., et al. 2021b, ApjL, 913, L7
Abbott, R., Abbott, T.D., Acernese, F., et al. 2021c, arXiv:2108.01045
Abbott, R., Abbott, T.D., Abraham, S., et al. 2021d, ApJL, 915, L5
Abbott, R., Abbott, T.D., Abraham, S., et al. 2021e, PhRvD, 103, 122002
Abbott, R., Abbott, T.D., Abraham, S., et al. 2021f, SoftX, 13, 100658
Abbott, R., Abbott, T.D., Acernese, F., et al. 2021g, arXiv:2111.03606
Abbott, R., Abbott, T.D., Acernese, F., et al. 2021h, arXiv:2111.03634
Abbott, R., Abbott, T.D., Acernese, F., et al. 2022, A&A, 659, A84
Acernese, F., Agathos, M., Agatsuma, K., et al. 2015, CQGra, 32, 024001
Acernese, F., Adams, T., Agatsuma, K, et al. 2018, CQGra, 35, 205004
Ade, P. A. R., Aghanim, N., Arnaud, M., et al. 2016, A&A, 594, A13
Ajith, P., Fotopoulos, N., Privitera, S., Neunzert, A., & Weinstein, A. J. 2014, PhRvD, 89, 084041
Akutsu, T., Ando, M., Arai, K., et al. 2021, PTEP, 2021, 05A101
Allen, B. 2005, PhRvD, 71, 062001
Allen, B., Anderson, W. G., Brady, P. R., Brown, D. A., & Creighton, J. D. E. 2012, PhRvD, 85, 122006
Andreoni, I., Anand, S., Bianco, F., et al. 2019, PASP, 131, 068004
Babak, S., Biswas, R., Brady, P., et al. 2013, PhRvD, 87, 024033
Bailyn, C. D., Jain, R. K., Coppi, P., & Orosz, J. A. 1998, ApJ, 499, 367
Belczynski, K., et al. 2016, A&A, 594, A97
Bhattacharjee, D., Lecoeuche, Y., Karki, S., et al. 2021, CQGra, 38, 015009
Biwer, C. M., Capano, C. D., De, S., et al. 2019, PASP, 131, 024503
Blanchet, L. 2002, LRR, 5, 3
Bohé, A., Shao, L., Taracchini, A., et al. 2017, PhRvD, 95, 044028
Burns, E., Goldstein, A., Hui, C. M., et al. 2019, ApJ, 871, 90
Cabero, M., Lundgren, A., Nitz, A. H., et al. 2019, CQGra, 36, 155010
Capano, C. D., Cabero, M., Westerweck, J., et al. 2021, arXiv:2105.05238
Carr, B., Clesse, S., García-Bellido, J., & Kühnel, F. 2021, PDU, 31, 100755
Chandra, K., Villa-Ortega, V., Dent, T., et al. 2021, PhRvD, 104, 042004
Clesse, S., & Garcia-Bellido, J. 2020, arXiv:2007.06481
Collaboration, L. S.Collaboration, V.Collaboration, K. 2021a, WTC-3: Compact Binary Coalescences Observed by LIGO and Virgo During the Second Part of the Third Observing Run Run -O3 search sensitivity estimates, Zenodo, doi:10.5281/zenodo.5546676
Collaboration, L. S., Collaboration, V., Collaboration, K. 2021b, Compact Binary Coalescences Observed by LIGO and Virgo During the Second Part of the Third Observing Run -O1+O2+O3 Search Sensitivity Estimates, Zenodo, doi:10.5281/zenodo.5636816
Countryman, S., Keivani, A., Bartos, I., et al. 2019, arXiv:1901.05486
Cromartie, H. T., Fonseca, E., Ransom, S. M., et al. 2020, NatAs, 4, 72
Dal Canton, T., & Harry, I. W. 2017, arXiv:1705.01845
Davies, G. S., Dent, T., Tápai, M., et al. 2020, PhRvD, 102, 022004
Davis, D., Massinger, T., Lundgren, A., et al. 2019, CQGra, 36, 055011
Davis, D., Areeda, J.S., Berger, B.K., et al. 2021, CQGra, 38, 135014
Dietrich, T., Bernuzzi, S., & Tichy, W. 2017, PhRvD, 96, 121501
Dietrich, T., Khan, S., Dudi, R., et al. 2019, PhRvD, 99, 024029
Droz, S., Knapp, D. J., Poisson, E., & Owen, B. J. 1999, PhRvD, 59, 124016
Edelman, B., Doctor, Z., & Farr, B. 2021, ApJL, 913, L23
Estevez, D., Lagabbe, P., Masserot, A., et al. 2021, CQGra, 38, 075007
Estevez, D., Mours, B., Rolland, L., & Verkindt, D. 2019, Online h(t) reconstruction for Virgo O3 data: start of O3, Tech. Rep. VIR-0652B-19, Virgo
Evans, M., Adhikari, R., Afle, C., et al. 2021, arXiv:2109.09882
Farr, W. M. 2019, RNAAS, 3, 66
Farr, W. M., Farr, B., & Littenberg, T. 2015a, Modelling Calibration Errors In CBC Waveforms, Tech. Rep. LIGO-T1400682, LIGO Project, T1400682
Farr, W. M., Gair, J. R., Mandel, I., & Cutler, C. 2015b, PhRv, 91, 023005
Farr, W. M., Sravan, N., Cantrell, A., et al. 2011, ApJ, 741, 103
Faye, G., Marsat, S., Blanchet, L., & Iyer, B. R. 2012, CQGra, 29, 175004
Fishbach, M., & Holz, D. E. 2020, ApJL, 904, L26
Fishbach, M., Holz, D. E., & Farr, W. M. 2018, ApJL, 863, L41
Fragione, G., & Banerjee, S. 2021, ApJL, 913, L29
Gerosa, D., & Fishbach, M. 2021, NatAs, 5, 8
Goldstein, A., et al. 2017, ApJL, 848, L14
Gupta, A., Gerosa, D., Arun, K. G., et al. 2020, PhRvD, 101, 103036
Harry, I., Calderón Bustillo, J., & Nitz, A. 2018, PhRvD, 97, 023004
Harry, I., Privitera, S., Bohé, A., & Buonanno, A. 2016, PhRvD, 94, 024012
Harry, I. W., Allen, B., & Sathyaprakash, B. 2009, PhRvD, 80, 104014
Husa, S., Khan, S., Hannam, M., et al. 2016, PhRvD, 93, 044006
Jeffreys, H. 1998, The Theory of Probability, Oxford Classic Texts in the Physical Sciences (Oxford: Oxford Univ. Press)
Kass, R. E., & Raftery, A. E. 1995, JASA, 90, 773
Khan, S., Husa, S., Hannam, M., et al. 2016, PhRvD, 93, 044007
Kimball, C., Talbot, C., L. Berry, C. P., et al. 2020, ApJ, 900, 177
Klimenko, S., Yakushin, I., Mercer, A., et al. 2008, CQGra, 25, 114029
Klimenko, S., Vedovato, G., Drago, M., et al. 2016, PhRvD, 93, 042004
LALSuite 2020, LSC Algorithm Library Suite, https://git.ligo.org/lscsoft/lalsuite
Liu, B., & Lai, D. 2021, MNRAS, 502, 2049
Loredo, T. J. 2004, in AIP Conf. Ser. 735, ed. R. Fischer, R. Preuss, & U. V. Toussaint (Melville, NY: AIP), 195
Lu, W., Beniamini, P., & Bonnerot, C. 2020, MNRAS, 500, 1817
Mandel, I., Farr, W. M., & Gair, J. R. 2019, MNRAS, 486, 1086
Marchant, P., Renzo, M., Farmer, R., et al. 2019, ApJ, 882, 36
Mozzon, S., Nuttall, L. K., Lundgren, A., et al. 2020, CQGra, 37, 215014
Nitz, A. H. 2018, CQGra, 35, 035016
Nitz, A. H., Capano, C. D., Kumar, S., et al. 2021a, ApJ, 922, 76
Nitz, A. H., & Capano, C. 2021, 3-OGC Open Gravitational-wave Catalog, GitHub,www.github.com/gwastro/3-ogc
Nitz, A. H., Dent, T., Dal Canton, T., Fairhurst, S., & Brown, D. A. 2017, ApJ, 849, 118
Nitz, A. H., Dent, T., Davies, G. S., & Harry, I. 2020, ApJ, 897, 169
Nitz, A. H., & Kumar, S. 2021, 4-OGC Open Gravitational-wave Catalog, GitHub, www.github.com/gwastro/4-ogc
Nitz, A. H., Lenon, A., & Brown, D. A. 2019a, ApJ, 890, 1
Nitz, A. H., Nielsen, A. B., & Capano, C. D. 2019b, ApJL, 876, L4
Nitz, A. H., & Wang, Y.-F. 2021a, PhRvL, 126, 021103
Nitz, A. H., & Wang, Y. F. 2021b, ApJ, 915, 54
Nitz, A. H., & Wang, Y.-F. 2021c, PhRvL, 127, 151101
Nitz, A. H., Dent, T., Davies, G. S., et al. 2019c, ApJ, 891, 123
Nitz, A. H., Harry, I. W., Willis, J. L., et al. 2021d, PyCBC Software, GitHub, https://github.com/gwastro/pycbc
Olejak, A., Fishbach, M., Belczynski, K., et al. 2020, ApJL, 901, L39
Özel, F., Psaltis, D., & Narayan, R. 1918, ApJ, 725, 1918
Pratten, G., Garcia-Quiros, C., Colleoni, M., et al. 2021, PhRvD, 103, 104056
Punturo, M., Abernathy, M., Acernese, F., et al. 2010, CQGra, 27, 194002
Ramos-Buades, A., Tiwari, S., Haney, M., & Husa, S. 2020, PhRvD, 102, 043005
Reitze, D., et al. 2019, BAAS, 51, 35
Rodriguez, C. L., Zevin, M., Amaro-Seoane, P., et al. 2019, PhRvD, 100, 043027
Rolland, L., Seglar-Arroyo, M., & Verkindt, D. 2019, Reprocessing of h(t) for the last two weeks of O3a, Tech. Rep. VIR-1201A-19, Virgo
Roulet, J., Chia, H. S., Olsen, S., et al. 2021, PhRvD, 104, 083010
Roulet, J., Venumadhav, T., Zackay, B., Dai, L., & Zaldarriaga, M. 2020, PhRvD, 102, 123022
Saleem, M., Rana, J., Gayathri, V., et al. 2022, CQGra, 39, 025004
Sathyaprakash, B. S., & Dhurandhar, S. V. 1991, PhRvD, 44, 3819
Savchenko, V., Ferrigno, C., Kuulkers, E., et al. 2017, ApJL, 848, L15
Setzer, C. N., Biswas, R., Peiris, H. V., et al. 2019, MNRAS, 485, 4260
Speagle, J. S. 2020, MNRAS, 493, 3132
Stevenson, S., Sampson, M., Powell, J., et al. 2019, ApJ, 882, 121
Stevenson, S., Sampson, M., Powell, J., et al. 2019, ApJ, 882, 121
Talbot, C., & Thrane, E. 2018, ApJ, 856, 173
Taracchini, A., Buonanno, A., Pan, Y., et al. 2014, PhRvD, 89, 061502
Thompson, J. E., Fauchon-Jones, E., Khan, S., et al. 2020, PhRvD, 101, 124059
Thrane, E., & Talbot, C. 2020, PASA, 37, e036
Tiwari, V. 2018, CQGra, 35, 145009
Tiwari, V., Klimenko, S., Christensen, N., et al. 2016, PhRvD, 93, 043007
Unnikrishnan, C. S. 2013, IJMPD, 22, 1341010
Usman, S. A., Nitz, A. H., Harry, I. W., et al. 2016, CQGra, 33, 215004
Vajente, G., Huang, Y., Isi, M., et al. 2020, PhRvD, 101, 042003
Vallisneri, M., Kanner, J., Williams, R., Weinstein, A., & Stephens, B. 2015, JPhCS, 610, 012021
van Son, L. A. C., De Mink, S. E., Broekgaarden, F. S., et al. 2020, ApJ, 897, 100
Venumadhav, T., Zackay, B., Roulet, J., Dai, L., & Zaldarriaga, M. 2020, PhRvD, 101, 083030
Venumadhav, T., Zackay, B., Roulet, J., Dai, L., & Zaldarriaga, M. 2019, PhRvD, 100, 023011
Viets, A. D., Wade, M., Urban, A. L., et al. 2018, CQGra, 35, 095015

Vitale, S., Gerosa, D., Farr, W. M., & Taylor, S. R. 2020, in Handbook of Gravitational Wave Astronomy, ed. C. Bambi, S. Katsanevas, & K. D. Kokkotas (Singapore: Springer)
Wang, Y.-F., Brown, S. M., Shao, L., & Zhao, W. 2022, PhRvD, 106, 084005
Wang, Y.-F., & Nitz, A. H. 2021, ApJ, 912, 53
Woosley, S. E. 2017, ApJ, 836, 244
Woosley, S. E. 2017, ApJ, 878, 49
Yoshida, T., Umeda, H., Maeda, K., & Ishii, T. 2016, MNRAS, 457, 351
Zevin, M., Spera, M., Berry, C. P. L., & Kalogera, V. 2020, ApJL, 899, L1
Zevin, M., Bavera, S. S., Berry, C. P. L., et al. 2021, ApJ, 910, 152
Zhu, J. P., Wu, S., Qin, Y., et al. 2022, ApJ, 928, 167
Zhu, J. P., Wu, S., Yang, Y. P., et al. 2021, ApJ, 921, 156
Ozel, F., & Freire, P. 2016, ARA&A, 54, 401